EIGHTEENTH EUROPEAN ROTORCRAFT FORUM

E - 12

Paper No. 29

AEROELASTIC MODELING OF COMPOSITE ROTOR BLADES WITH STRAIGHT AND SWEPT TIPS

Kuo-An Yuan
Peretz P. Friedmann and Comandur Venkatesan

Mechanical, Aerospace, and Nuclear Engineering Department
University of California, Los Angeles
Los Angeles, CA 90024-1597, U.S.A.

September 15-18, 1992

Avignon, France

ASSOCIATION AERONAUTIQUE ET ASTRONAUTIQUE DE FRANCE

AEROELASTIC MODELING OF COMPOSITE ROTOR BLADES WITH STRAIGHT AND SWEPT TIPS

Kuo-An Yuan†
Peretz P. Friedmann* and Comandur Venkatesan**
Mechanical, Aerospace, and Nuclear Engineering Department
University of California, Los Angeles
Los Angeles, CA 90024-1597, U.S.A.

Abstract

This paper presents an analytical study of the aeroelastic behavior of composite rotor blades with straight and swept tips. The blade is modeled by beam type finite elements. A single finite element is used to model the swept tip. The nonlinear equations of motion for the finite element model are derived using Hamilton's principle and based on a moderate deflection theory and accounts for: arbitrary cross-sectional shape, pretwist, generally anisotropic material behavior, transverse shears and out-of-plane warping. Numerical results illustrating the effects of tip sweep, anhedral and composite ply orientation on blade aeroelastic behavior are presented. It is shown that composite ply orientation has a substantial effect on blade stability. At low thrust conditions, certain ply orientations can cause instability in the lag mode. The flap-torsion coupling associated with tip sweep can also induce aeroelastic instability in the blade. This instability can be removed by appropriate ply orientation in the composite construction. These results illustrate the inherent potential for aeroelastic tailoring present in composite rotor blades with swept tips, which still remains to be exploited in the design process.

Nomenclature

a	Lift curve slope
B	Number of blades
c	Airfoil chord
C_{d_0}	Blade profile drag coefficient
$C_{ij}(i, j = 1, \ldots, 6)$	Material elastic moduli
C_T	Thrust coefficient of rotor
C_W	Weight coefficient of helicopter
$[C]$	Damping matrix
e_1	Blade root offset
$\hat{e}_x, \hat{e}_y, \hat{e}_z$	Orthonormal triad of element coordinate system
$\hat{e}_x, \hat{e}_\eta, \hat{e}_\zeta$	Orthonormal triad of undeformed curvilinear coordinate system
$\hat{e}'_x, \hat{e}'_\eta, \hat{e}'_\zeta$	Orthonormal triad of deformed curvilinear coordinate system
$\mathbf{E}_x, \mathbf{E}_\eta, \mathbf{E}_\zeta$	Base vectors of deformed elastic axis
E_L	Longitudinal Young's modulus
E_T	Transverse Young's modulus

† Research Assistant
* Professor
** Associate Research Engineer

γ_{ij}	Strain tensor in curvilinear coordinates
$\mathbf{F}$	Load vector in equations of motion
g_x, g_η, g_ζ	Base vectors of undeformed beam
G_x, G_η, G_ζ	Base vectors of deformed beam
G_{LT}	Longitudinal shear modulus
h_e	Offset of beam element in-board node from blade root
$\hat{i}_b$, $\hat{j}_b$, $\hat{k}_b$	Orthonormal triad of preconed, pitched, blade-fixed coordinate system
$\hat{i}_{nr}$, $\hat{j}_{nr}$, $\hat{k}_{nr}$	Orthonormal triad of nonrotating, hub-fixed coordinate system
$\hat{i}_r$, $\hat{j}_r$, $\hat{k}_r$	Orthonormal triad of rotating, hub-fixed coordinate system
$[K]$	Stiffness matrix
l_e	Length of beam element
$[M]$	Mass matrix
$\mathbf{P}$	Distributed force vector along elastic axis
$\mathbf{q}$	Vector of finite element nodal degrees of freedom
$\mathbf{Q}$	Distributed moment vector along elastic axis
$\mathbf{r}$	Position vector of undeformed beam
R	Rotor radius
$\mathbf{R}$	Position vector of deformed beam
$\mathbf{R}_0$	Position vector of deformed elastic axis
T	Kinetic energy
$[T_{rn}]$,$[T_{br}]$,$[T_{eb}]$, $[T_{ce}]$,$[T_{dc}]$,$[T_{de}]$	Transformation matrices between coordinate systems
u, v, w	Displacement components in $(\hat{e}_x, \hat{e}_y, \hat{e}_z)$ system
U	Strain energy
$\mathbf{V}$	Velocity vector of a point on rotating blade
W_e	Work of nonconservative loads
x, η, ζ	Curvilinear coordinates
x_1, x_2, x_3	Indicial notations for x, η and ζ
y_1, y_2, y_3	Local cartesian coordinates
$\mathbf{y}$	Vector of generalized coordinates in modal space
$\mathbf{y}_0$	Nonlinear equilibrium position in hover
α	Amplitude of warping
β	Pretwist angle of beam
β_p	Blade precone angle
γ	Lock number
$\gamma_{\eta\zeta}$, $\gamma_{x\zeta}$, $\gamma_{x\eta}$	Shear strain components
$\bar{\gamma}_{x\eta}$, $\bar{\gamma}_{x\zeta}$	Transverse shears at elastic axis
$\delta\mathbf{u}$	Virtual displacement vector of elastic axis
$\delta\vec{\Theta}$	Virtual rotation vector of elastic axis
ε	Non-dimensional parameter representing order of magnitude of typical elastic blade slope
ε_{xx}, $\varepsilon_{\eta\eta}$, $\varepsilon_{\zeta\zeta}$	Normal strain components
$\bar{\varepsilon}_{xx}$	Axial strain at elastic axis
θ_p	Blade pitch angle due to control pitch setting, $\theta_p = \theta_0$ for hover
θ_x, θ_η, θ_ζ	Euler angles in the transformation between the $(\hat{e}'_x, \hat{e}'_\eta, \hat{e}'_\zeta)$ system and the $(\hat{e}_x, \hat{e}_\eta, \hat{e}_\zeta)$ system

θ_0	Collective pitch
κ_η, κ_ζ	Curvatures of the deformed beam
$[K]$	Transformation matrix between $(\hat{c}'_x, \hat{c}'_\eta, \hat{c}'_\zeta)$ and its derivatives
$[K_0]$	Transformation matrix between $(\hat{c}_x, \hat{c}_\eta, \hat{c}_\zeta)$ and its derivatives
Λ_a	Tip anhedral angle, positive upward
Λ_s	Tip sweep angle, positive backward
Λ_v, Λ_h	Ply angle in vertical walls and horizontal walls, respectively, for composite blades
$[\Lambda]$	Local-to-global transformation matrix for swept tip
ν_{LT}	Longitudinal Poisson's ratio
ρ	Mass density of beam
σ	Rotor solidity
$\sigma_{xx}, \sigma_{\eta\eta}, \sigma_{\zeta\zeta}$	Normal stress components
$\sigma_{\eta\zeta}, \sigma_{x\zeta}, \sigma_{x\eta}$	Shear stress components .
τ	Twist of deformed beam
τ_0	Initial twist of the beam ($= \beta_{,x}$)
ϕ	Elastic twist angle of blade
ϕ_0	Second order term of deformed twist, Eq. (23)
ψ	Blade azimuth ($= \Omega t$)
Ψ	Out-of-plane warping function
ω_{L1}, ω_{F1}, ω_{T1}	Fundamental rotating lag, flap and torsional blade frequencies
Ω	Angular velocity of rotor
$(\ )_{,x}(\ )_{,\eta}(\ )_{,\zeta}$	Derivatives of ( ) with respect to x, η, ζ , respectively
$\delta(\ )$	Variation of ( )

1. Introduction

In recent years, most helicopter rotor blades have been built of composite materials, because such blades have better fatigue life and damage tolerance than metal blades. Furthermore, the manufacturing processes for composite blades provide the designer with the freedom to incorporate more refined planforms and airfoil geometries. Composite rotor blades also offer the potential for aeroelastic tailoring which can produce remarkable payoff in the multidisciplinary design of rotorcraft.

Numerous blade models developed to date have been restricted to isotropic material properties[1-7] . During the past few years, a substantial number of analytical studies have been aimed at the development of models which are suitable for the structural and aeroelastic analysis of composite rotor blades. The important attributes of such a structural model is the capability to represent transverse shear deformation, cross-sectional warping and elastic coupling, in addition to an adequate representation of geometric nonlinearities. A review of the existing structural models suitable for modeling composite rotor blades were presented by Friedmann[8] and Hodges[9]. There are two types of theories for composite rotor blade structural modeling depending on the level of geometric nonlinearities being retained in the one-dimensional beam kinematics. The first type is based on a moderate deflection theory[10-13] while the second type is capable of modeling large deflections[14-18] . Moderate deflection theories usually use an ordering scheme to limit the magnitude of blade displacements and rotations, thus enable the strain-displacement relations and the transformation between the deformed and undeformed coordinates be expressed in terms of blade displacement quantities (u,

v, w, ϕ, and their derivatives with respect to the axial coordinate, x) explicitly. While large deflection theories do not utilize an ordering scheme to limit the magnitude of blade displacements and rotations. The only assumption used to neglect higher order terms in such theories is that the strains are small.

For helicopter rotor blades aeroelastic analysis, moderate deflection theories are usually adequate provided that a consistent ordering scheme is used. Blade models based on large deflection theories are mathematically more elegant and more consistent than those using an ordering scheme; however, the incorporation of such models into general aeroelastic analysis models is more complicated. Also such models may be computationally less efficient and the results may be more difficult to interpret.

To date, the only published body of research on composite rotor blades which actually contains aeroelastic stability and response type of results is that published by Chopra and his associates[10-12] which is based on a moderate deflection theory. The strain-displacement relations in this model were taken from Hodges and Dowell[1], which does not include the effect of transverse shear deformations. Also, the model is restricted to a specific cross-sectional shape, i.e., a single-cell, rectangular box beam for a hingeless blade. Therefore, the important requirement for the development of a general aeroelastic analysis capability suitable for composite rotor blades with arbitrary cross-sectional geometry, remains essentially unfulfilled.

Rotor blades with swept tips, shown schematically in Fig. 1, have also received considerable attention in recent years. Swept tips introduce bending-torsion and bending-axial coupling effects which have significant influence on blade dynamics because they are located at the regions of high dynamic pressure and relatively large displacements. Tip sweep and tip anhedral also provide another means for the aeroelastic tailoring of rotor blades. Furthermore, swept tips are also effective for reducing aerodynamic noise and blade vibrations. Only a limited number of analytical studies have addressed the aeroelastic modeling of rotor blades with swept tips[19-21] ; among these Reference 20 represents a reasonably comprehensive study. However, all these studies were restricted to isotropic blades. Despite its comprehensive nature, the model used in Ref. 20 approximated the swept tip portion of the blade as axially rigid and it also employed a linear transformation in the assembly of the swept-tip element with the straight portion of the blade. Such a transformation could be inaccurate for large sweep angles[22] .

The ultimate goal of this study is the structural optimization and aeroelastic tailoring of composite rotor blades with swept tips. For this class of studies computational efficiency is a primary concern; and therefore it was necessary to develop the moderate deflection composite blade model presented in this paper. The primary objectives of this study are:

1. Development of a new aeroelastic model for composite rotor blades with straight and swept tips, based on a moderate deflection theory, which is suitable for aeroelastic tailoring and structural optimization studies due to its computational efficiency.
2. To study the effects of tip sweep and tip anhedral on the aeroelastic response and stability of an isotropic rotor blade in hover, since the relative importance of these two effects has not been carefully studied before.
3. To study the effects of ply orientation on the aeroelastic stability of a straight composite rotor blade in hover, for both single-cell and double-cell blade configurations.
4. To examine the combined effects of tip sweep and ply orientation on the aeroelastic stability of a composite rotor blade with a swept tip in hover.

The numerical results presented in the paper illustrate the aeroelastic behavior of swept composite rotor blades in hover; these results, which have not been presented in the literature before, demonstrate the inherent potential of swept-tip composite blade configurations for aeroelastic tailoring.

2. Formulation of the Blade Model

The hingeless composite rotor blade is modeled as an elastic rotating beam with constant angular velocity Ω. It consists of a straight portion and a swept tip whose orientation relative to the straight portion is described by a sweep angle (Λ_s) and an anhedral angle (Λ_a) . The cross-section of the blade has a general shape with distinct shear center, tension center and center of mass. Precone, control pitch setting, pretwist and root offset are included in this model. The blade is modeled by a series of straight beam finite elements along the elastic axis of the blade. A single finite element is used to model the swept tip. The nonlinear strain-displacement relations are derived assuming a moderate deflection theory (small strains and finite rotations) with appropriate provision for transverse shear deformations and out-of-plane warping. Hamilton's principle is used in the derivation of the nonlinear equations of motion and the corresponding finite element matrices for each beam element.

2.1 Coordinate Systems

Several coordinate systems are required to fully describe the geometry and deformation of the blade. Each coordinate system is symbolically represented by a set of orthonormal triad. The first three systems, namely, the nonrotating, hub-fixed system $(\hat{i}_{nr}, \hat{j}_{nr}, \hat{k}_{nr})$, the rotating, hub-fixed system $(\hat{i}_r, \hat{j}_r, \hat{k}_r)$, and the preconed, pitched, blade-fixed system $(\hat{i}_b, \hat{j}_b, \hat{k}_b)$, respectively, are used to position and orient the blade relative to the hub through rigid-body motions, as shown in Figs. 2 and 3. The $(\hat{i}_r, \hat{j}_r, \hat{k}_r)$ system rotates with a constant angular velocity $\Omega\hat{k}_r$; while the $(\hat{i}_b, \hat{j}_b, \hat{k}_b)$ system is offset from the $(\hat{i}_r, \hat{j}_r, \hat{k}_r)$ system by $e_1\hat{i}_r$, and oriented by rotating the $(\hat{i}_r, \hat{j}_r, \hat{k}_r)$ system about $-\hat{j}_r$ by the precone angle β_p and then about the rotated $\hat{i}_r$ by the pitch angle θ_p. In the finite element model of the blade, the $(\hat{i}_b, \hat{j}_b, \hat{k}_b)$ system is the global coordinate system.

The next two systems, $(\hat{e}_x, \hat{e}_y, \hat{e}_z)$ and $(\hat{e}_x, \hat{e}_\eta, \hat{e}_\zeta)$, respectively, are used to position and orient each beam finite element relative to the $(\hat{i}_b, \hat{j}_b, \hat{k}_b)$ system in the undeformed configuration of the blade, as shown in Figs. 4 and 5. The vector $\hat{e}_x$ is aligned with the beam element elastic axis; while the vectors $\hat{e}_y$ and $\hat{e}_z$ are defined in the cross-section of the beam. For the straight portion of the blade, the $(\hat{e}_x, \hat{e}_y, \hat{e}_z)$ system has the same orientation as the $(\hat{i}_b, \hat{j}_b, \hat{k}_b)$ system. For the swept-tip element, the $(\hat{e}_x, \hat{e}_y, \hat{e}_z)$ system is oriented by rotating the $(\hat{i}_b, \hat{j}_b, \hat{k}_b)$ system about $-\hat{k}_b$ by the sweep angle Λ_s and then about $-\hat{j}_b$ by the anhedral angle Λ_a . The $(\hat{e}_x, \hat{e}_y, \hat{e}_z)$ system is also the local coordinate system for the blade finite element model. Effects of blade pretwist are properly accounted for by deriving the beam element strain-displacement relations in the $(\hat{e}_x, \hat{e}_\eta, \hat{e}_\zeta)$ system, which rotates with the beam pretwist. The vectors $\hat{e}_\eta$ and $\hat{e}_\zeta$ are defined parallel to the modulus weighted principal axes of the cross section; and the pretwist angle $\beta(x)$ is defined as the change in the orientation of $\hat{e}_\eta, \hat{e}_\zeta$ with respect to $\hat{e}_y, \hat{e}_z$, respectively, at any location along the beam element, as shown in Fig. 5.

A final system, $(\hat{c}'_x, \hat{c}'_\eta, \hat{c}'_\zeta)$, is used to represent the orientation of the local blade geometry after deformation. The orientation of the $(\hat{c}'_x, \hat{c}'_\eta, \hat{c}'_\zeta)$ system is obtained by rotating the $(\hat{c}_x, \hat{c}_\eta, \hat{c}_\zeta)$ system through three Euler angles in the order of θ_ζ, θ_η and θ_x about $\hat{c}_\zeta$, rotated $\hat{c}_\eta$ and rotated $\hat{c}_x$, respectively. This sequence was chosen to follow the work of previous authors[1-3], but other sequences are also possible. The vector $\hat{c}'_x$ is chosen to be tangent to the local deformed elastic axis[23]. The transformation matrices between various coordinate systems are shown in Appendix A.

2.2 Structural Modeling

In this study, the nonlinear kinematics of deformation is based on the mechanics of curved rods[23,24]. The strain components are first derived in a curvilinear coordinate system so that the effects of pretwist is properly accounted for. These strain components are then transformed to a local cartesian coordinate system. The stress-strain relations are assumed to be defined in this local cartesian coordinate system. The kinematical assumptions used in the derivation are: (1) the deformations of the cross section in its own plane are neglected; (2) the strain components are small compared to unity and no assumption is made regarding the relative magnitude between the axial and shear strains; and (3) higher order warping terms are neglected.

2.2.1 Kinematics of Deformation

The position vector of a point P on the undeformed beam is written as

$$r(x, \eta, \zeta) = e_1 \hat{i}_r + h_e \hat{i}_b + x\hat{c}_x + \eta\hat{c}_\eta + \zeta\hat{c}_\zeta \tag{1}$$

Equation (1) can be used to represent the undeformed position vector both for a point on the straight portion as well as a point on the swept-tip portion. For a point on the swept-tip element, h_e equals the length of the straight portion of the blade. The corresponding undeformed base vectors at point P are defined by

$$g_x = r_{,x} = \hat{c}_x - \zeta\tau_0\hat{c}_\eta + \eta\tau_0\hat{c}_\zeta \tag{2a}$$

$$g_\eta = r_{,\eta} = \hat{c}_\eta \tag{2b}$$

$$g_\zeta = r_{,\zeta} = \hat{c}_\zeta \tag{2c}$$

where the derivatives of the orthonormal triad $(\hat{c}_x, \hat{c}_\eta, \hat{c}_\zeta)$ are related to the initial twist, τ_0, of the undeformed beam by

$$\begin{Bmatrix} \hat{c}_{x,x} \\ \hat{c}_{\eta,x} \\ \hat{c}_{\zeta,x} \end{Bmatrix} = \begin{bmatrix} 0 & 0 & 0 \\ 0 & 0 & \tau_0 \\ 0 & -\tau_0 & 0 \end{bmatrix} \begin{Bmatrix} \hat{c}_x \\ \hat{c}_\eta \\ \hat{c}_\zeta \end{Bmatrix} \tag{3}$$

and

$$\tau_0 = \beta_{,x} \tag{4}$$

Since the in-plane deformations of the beam cross-section are neglected, the position vector of the point P in the deformed configuration can be written as

$$R(x, \eta, \zeta) = R_0(x) + \eta E_\eta + \zeta E_\zeta + \alpha(x)\Psi(\eta, \zeta)\hat{e}'_x \tag{5}$$

where

$$R_0(x) = R(x, 0, 0) \tag{6}$$

is the corresponding position vector of a point on the deformed elastic axis; and

$$E_i(x) = R_{,i}(x, 0, 0), \qquad i = x, \eta, \zeta \tag{7}$$

are the base vectors of a point on the deformed elastic axis. In Eq. (5), the first three terms represent translations and rotations of the cross-section, while the last term is the out-of-plane warping of the cross-section. $\alpha(x)$ is the unknown amplitude of warping; $\Psi(\eta, \zeta)$ is the out-of-plane warping function of the cross-section, with $\Psi(0, 0) = \Psi_{,\eta}(0, 0) = \Psi_{,\zeta}(0, 0) = 0$. Without loss of generality, the unit vector $\hat{e}'_x$ is assumed to be in the direction of E_x, i.e., tangent to the deformed elastic axis; while the orientations of $\hat{e}'_\eta$ and $\hat{e}'_\zeta$ are nearly that of E_η and E_ζ but differ on account of the strains[23] . With the assumption that in-plane deformations of the beam cross-section are neglected, the base vectors of the deformed elastic axis are expressed by the following definition[23]

$$E_x = (1 + \bar{\varepsilon}_{xx})\hat{e}'_x \tag{8a}$$

$$E_\eta = \bar{\gamma}_{x\eta}\hat{e}'_x + \hat{e}'_\eta \tag{8b}$$

$$E_\zeta = \bar{\gamma}_{x\zeta}\hat{e}'_x + \hat{e}'_\zeta \tag{8c}$$

where $\bar{\varepsilon}_{xx}$, $\bar{\gamma}_{x\eta}$ and $\bar{\gamma}_{x\zeta}$ can be shown to be the axial and the transverse shear strains, respectively, at the elastic axis[23] . The deformed base vectors at point P are defined as

$$G_x = R_{,x}, \quad G_\eta = R_{,\eta}, \quad G_\zeta = R_{,\zeta} \tag{9}$$

where the derivatives of the orthonormal triad $(\hat{e}'_x, \hat{e}'_\eta, \hat{e}'_\zeta)$ are related to the curvatures, $\kappa_\eta, \kappa_\zeta$, and twist, τ , of the deformed beam by

$$\begin{Bmatrix} \hat{e}'_{x,x} \\ \hat{e}'_{\eta,x} \\ \hat{e}'_{\zeta,x} \end{Bmatrix} = \begin{bmatrix} 0 & \kappa_\eta & \kappa_\zeta \\ -\kappa_\eta & 0 & \tau \\ -\kappa_\zeta & -\tau & 0 \end{bmatrix} \begin{Bmatrix} \hat{e}'_x \\ \hat{e}'_\eta \\ \hat{e}'_\zeta \end{Bmatrix} \tag{10}$$

2.2.2 Strain Components

The set of coordinates (x, η, ζ) are, in general, non-orthogonal curvilinear coordinates since the base vector g_x, expressed in Eq. (2a) is neither a unit vector nor orthogonal to the base vectors g_η and g_ζ for an arbitrary point on the beam with nonzero initial twist τ_0. In the derivation that follows, the notations (x_1, x_2, x_3) will be used in place of (x, η, ζ) whenever convenient.

The components of the strain tensor in the curvilinear coordinates are defined by[24]

$$f_{ij} = \frac{1}{2}(G_i \cdot G_j - g_i \cdot g_j), \quad i, j = x, \eta, \zeta \tag{11}$$

Define a system of local cartesian coordinates (y_1, y_2, y_3) at point P with its unit vectors parallel to the orthonormal triad $(\hat{e}_x, \hat{e}_\eta, \hat{e}_\zeta)$ of the cross section, respectively. The stress-strain relations of the beam are assumed to be given in the local cartesian coordinate system. The transformation relation between the curvilinear coordinates (x_1, x_2, x_3) and the local cartesian coordinates (y_1, y_2, y_3) is given[24] in matrix form by

$$\left[\frac{\partial x_i}{\partial y_j}\right] = [g_k \cdot g_i]^{-1}[g_k \cdot \hat{e}_j] = \begin{bmatrix} 1 & 0 & 0 \\ \zeta\tau_0 & 1 & 0 \\ -\eta\tau_0 & 0 & 1 \end{bmatrix} \tag{12}$$

The strain tensor defined in the local cartesian coordinates, ε_{ij}, is obtained from the transformation

$$\varepsilon_{ij} = \sum_{k=1}^{3}\sum_{l=1}^{3} \frac{\partial x_k}{\partial y_i}\frac{\partial x_l}{\partial y_j} f_{kl} \tag{13}$$

Combining Eqs. (2), (5), and (8) through (13), the strain components in the local cartesian coordinates become

$$\begin{aligned} \varepsilon_{xx} = {} & \bar{\varepsilon}_{xx} - \eta\kappa_\eta - \zeta\kappa_\zeta + \alpha_{,x}\Psi + \alpha\tau_0(\zeta\Psi_{,\eta} - \eta\Psi_{,\zeta}) \\ & + \frac{1}{2}(\eta^2 + \zeta^2)(\tau - \tau_0)^2 + \eta(\bar{\gamma}_{x\eta,x} - \tau_0\bar{\gamma}_{x\zeta}) \\ & + \zeta(\bar{\gamma}_{x\zeta,x} + \tau_0\bar{\gamma}_{x\eta}) \end{aligned} \tag{14a}$$

$$\gamma_{x\eta} = \bar{\gamma}_{x\eta} + \alpha\Psi_{,\eta} - \zeta(\tau - \tau_0) \tag{14b}$$

$$\gamma_{x\zeta} = \bar{\gamma}_{x\zeta} + \alpha\Psi_{,\zeta} + \eta(\tau - \tau_0) \tag{14c}$$

$$\varepsilon_{\eta\eta} \simeq \varepsilon_{\zeta\zeta} \simeq \gamma_{\eta\zeta} \simeq 0 \tag{14d - f}$$

where

$$\gamma_{x\eta} \equiv 2\varepsilon_{x\eta}\,, \quad \gamma_{x\zeta} \equiv 2\varepsilon_{x\zeta}\,, \quad \gamma_{\eta\zeta} \equiv 2\varepsilon_{\eta\zeta}$$

The strain components in Eqs. (14a-c) are valid for small strains and large deflections and are expressed in terms of seven unknown functions of the axial coordinate x: $\bar{\varepsilon}_{xx}$, $\bar{\gamma}_{x\eta}$, $\bar{\gamma}_{x\zeta}$, κ_η, κ_ζ, τ and α. The first three are the axial and transverse shear strains, respectively, at the elastic axis; the next three are curvatures and twist, respectively, of the deformed beam; α is the amplitude of warping.

In developing an aeroelastic model, it is desirable to express the strain components in terms of the displacement components (u, v, w) of the elastic axis and the elastic twist (ϕ) so that the structural model can be more conveniently combined with the inertial and aerodynamic models. To accomplish this, we need to eliminate four of the seven unknowns in Eq. (14) by relating them to u, v, w and ϕ. An ordering scheme[8] was used to simplify these relations by neglecting terms of order ε^2 with respect to terms of order 1. It is assumed that rotation terms such as $v_{,x}$, $w_{,x}$ and ϕ are of order ε, while strain terms such as $u_{,x}$, $\bar{\gamma}_{x\eta}$ and $\bar{\gamma}_{x\zeta}$ are of order ε^2. The warping amplitude α is assumed to have the same order of magnitude as $\phi_{,x}$. This scheme is consistent with a moderate deflection theory (small strains and moderate rotations). Writing the vector $\mathbf{E}_x$ as

$$\mathbf{E}_x = (1 + u_{,x})\hat{e}_x + v_{,x}\hat{e}_y + w_{,x}\hat{e}_z = (1 + \bar{\varepsilon}_{xx})\hat{e}'_x \tag{15}$$

Equating the magnitude of $\mathbf{E}_x$ in Eq. (15) and applying the ordering scheme, as well as the small strain assumption, give

$$\bar{\varepsilon}_{xx} = u_{,x} + \frac{1}{2}(v_{,x})^2 + \frac{1}{2}(w_{,x})^2 \tag{16}$$

The deformed curvatures and twist can be related to the Euler angles (θ_x, θ_η, θ_ζ) by differentiating Eq. (A.5) with respect to x and combining with Eq. (3)

$$\begin{Bmatrix} \hat{e}'_{x,x} \\ \hat{e}'_{\eta,x} \\ \hat{e}'_{\zeta,x} \end{Bmatrix} = \left([T_{dc}]_{,x} + [T_{dc}][K_0]\right)\begin{Bmatrix} \hat{e}_x \\ \hat{e}_\eta \\ \hat{e}_\zeta \end{Bmatrix} \tag{17}$$

which yields

$$[K] = \left([T_{dc}]_{,x} + [T_{dc}][K_0]\right)[T_{dc}]^T \tag{18}$$

by combining Eqs. (17) and (10). where

$$[K_0] \equiv \begin{bmatrix} 0 & 0 & 0 \\ 0 & 0 & \tau_0 \\ 0 & -\tau_0 & 0 \end{bmatrix} \tag{19}$$

$$[K] \equiv \begin{bmatrix} 0 & \kappa_\eta & \kappa_\zeta \\ -\kappa_\eta & 0 & \tau \\ -\kappa_\zeta & -\tau & 0 \end{bmatrix} \tag{20}$$

Writing the vector E_x in the $(\hat{e}_x, \hat{e}_\eta, \hat{e}_\zeta)$ system, using Eqs. (15) and (A.4)

$$E_x = (1 + u_{,x})\hat{e}_x + (v_{,x}\cos\beta + w_{,x}\sin\beta)\hat{e}_\eta + (w_{,x}\cos\beta - v_{,x}\sin\beta)\hat{e}_\zeta \tag{21}$$

The deformation of an element dx on the beam elastic axis is then described in Fig. 6, where the effects of the rigid-body translation are not shown. The expressions for the deformed curvatures and twist in terms of v, w and ϕ are obtained by combining Eq. (18) and the trigonometric relations derived from Fig. 6 and applying the ordering scheme

$$\kappa_\eta = v_{,xx}\cos(\beta + \phi) + w_{,xx}\sin(\beta + \phi) \tag{22a}$$

$$\kappa_\zeta = -v_{,xx}\sin(\beta + \phi) + w_{,xx}\cos(\beta + \phi) \tag{22b}$$

$$\tau = \tau_0 + \phi_{,x} + \phi_0 \tag{22c}$$

where

$$\phi_0 = (-v_{,x}\sin\beta + w_{,x}\cos\beta)(v_{,xx}\cos\beta + w_{,xx}\sin\beta) \tag{23}$$

In Eqs. (22a-c), the torsional twist angle θ_x is replaced by ϕ, in order to be consistent with the usual notation in the literature. The non-zero strain components in Eqs. (14) can now be expressed in terms of u, v, w and ϕ by substituting Eqs. (16) and (22a-c) into Eqs. (14) and applying the ordering scheme.

$$\begin{aligned}\varepsilon_{xx} = {} & u_{,x} + \frac{1}{2}(v_{,x})^2 + \frac{1}{2}(w_{,x})^2 - v_{,xx}[\eta\cos(\beta + \phi) - \zeta\sin(\beta + \phi)] - \\ & w_{,xx}[\eta\sin(\beta + \phi) + \zeta\cos(\beta + \phi)] + \frac{1}{2}(\eta^2 + \zeta^2)(\phi_{,x})^2 + \\ & \alpha_{,x}\Psi + \alpha\tau_0(\zeta\Psi_{,\eta} - \eta\Psi_{,\zeta}) + \eta(\bar{\gamma}_{x\eta,x} - \tau_0\bar{\gamma}_{x\zeta}) + \zeta(\bar{\gamma}_{x\zeta,x} + \tau_0\bar{\gamma}_{x\eta})\end{aligned} \tag{24a}$$

$$\gamma_{x\eta} = \bar{\gamma}_{x\eta} + \alpha\Psi_{,\eta} - \zeta(\phi_{,x} + \phi_0) \tag{24b}$$

$$\gamma_{x\zeta} = \bar{\gamma}_{x\zeta} + \alpha\Psi_{,\zeta} + \eta(\phi_{,x} + \phi_0) \tag{24c}$$

The seven unknown functions of the axial coordinate, x , in the strain-displacement relations, Eqs. (24a-c), become: u, v, w, ϕ, α, $\bar{\gamma}_{x\eta}$ and $\bar{\gamma}_{x\zeta}$.

2.2.3 Constitutive Relations

The constitutive relations are defined based on the assumptions that the material properties are linear elastic and generally orthotropic (anisotropic behavior) and that the stress components within the cross section are set to zero ($\sigma_{\eta\eta} = \sigma_{\zeta\zeta} = \sigma_{\eta\zeta} = 0$) . The anisotropic stress-strain relations for a linearly elastic body are written as

$$\begin{bmatrix} \sigma_{xx} \\ \sigma_{\eta\eta} \\ \sigma_{\zeta\zeta} \\ \sigma_{\eta\zeta} \\ \sigma_{x\zeta} \\ \sigma_{x\eta} \end{bmatrix} = \begin{bmatrix} C_{11} & C_{12} & C_{13} & C_{14} & C_{15} & C_{16} \\ C_{12} & C_{22} & C_{23} & C_{24} & C_{25} & C_{26} \\ C_{13} & C_{23} & C_{33} & C_{34} & C_{35} & C_{36} \\ C_{14} & C_{24} & C_{34} & C_{44} & C_{45} & C_{46} \\ C_{15} & C_{25} & C_{35} & C_{45} & C_{55} & C_{56} \\ C_{16} & C_{26} & C_{36} & C_{46} & C_{56} & C_{66} \end{bmatrix} \begin{bmatrix} \varepsilon_{xx} \\ \varepsilon_{\eta\eta} \\ \varepsilon_{\zeta\zeta} \\ \gamma_{\eta\zeta} \\ \gamma_{x\zeta} \\ \gamma_{x\eta} \end{bmatrix} \tag{25}$$

Setting the three stress components within the cross section equal to zero and applying back substitution, the constitutive relations are

$$\begin{Bmatrix} \sigma_{xx} \\ \sigma_{x\zeta} \\ \sigma_{x\eta} \end{Bmatrix} = \begin{bmatrix} Q_{11} & Q_{15} & Q_{16} \\ Q_{15} & Q_{55} & Q_{56} \\ Q_{16} & Q_{56} & Q_{66} \end{bmatrix} \begin{Bmatrix} \varepsilon_{xx} \\ \gamma_{x\zeta} \\ \gamma_{x\eta} \end{Bmatrix} \tag{26}$$

where

$$[Q] = [C_{bb}] - [C_{bs}][C_{ss}]^{-1}[C_{sb}]$$

$$[C_{bb}] = \begin{bmatrix} C_{11} & C_{15} & C_{16} \\ C_{15} & C_{55} & C_{56} \\ C_{16} & C_{56} & C_{66} \end{bmatrix}$$

$$[C_{ss}] = \begin{bmatrix} C_{22} & C_{23} & C_{24} \\ C_{23} & C_{33} & C_{34} \\ C_{24} & C_{34} & C_{44} \end{bmatrix}$$

$$[C_{bs}] = [C_{sb}]^T = \begin{bmatrix} C_{12} & C_{13} & C_{14} \\ C_{25} & C_{35} & C_{45} \\ C_{26} & C_{36} & C_{46} \end{bmatrix}$$

2.3 Aerodynamic Modeling

The aerodynamic loads are obtained using Greenberg's theory with a quasi-steady assumption. Stall and compressibility effects are neglected. The induced inflow is assumed to be uniform and steady. The implementation of this aerodynamic model is based on an implicit formulation[25] where the expressions used in the derivation of the aerodynamic loads are coded in the computer program and assembled numerically during the solution process. Explicit algebraic form of the aerodynamic loads as a function of the displacement variables is not required; and the ordering scheme is not used in this implicit formulation. Furthermore this formulation of the unsteady aerodynamic loads enables one to replace the simple theory used here by more refined theories without an excessive amount of additional effort.

2.4 Hamilton's Principle

The nonlinear equations of motion and the corresponding finite element matrices are derived for each beam element using Hamilton's principle

$$\int_{t_1}^{t_2} (\delta U - \delta T - \delta W_e)\, dt = 0 \tag{27}$$

where δU, δT and δW_e represent the strain energy variation, kinetic energy variation, and virtual work of external loads, respectively.

2.4.1 Strain Energy

The variation of the strain energy for each beam element is

$$\delta U = \int_0^{l_e} \iint_A \begin{Bmatrix} \delta\varepsilon_{xx} \\ \delta\gamma_{x\zeta} \\ \delta\gamma_{x\eta} \end{Bmatrix}^T \begin{bmatrix} Q_{11} & Q_{15} & Q_{16} \\ Q_{15} & Q_{55} & Q_{56} \\ Q_{16} & Q_{56} & Q_{66} \end{bmatrix} \begin{Bmatrix} \varepsilon_{xx} \\ \gamma_{x\zeta} \\ \gamma_{x\eta} \end{Bmatrix} d\eta d\zeta dx \tag{28}$$

Integrating Eq. (28) over the cross section yields three sets of modulus weighted section constants, which are presented in Appendix B. These section constants are calculated by a separate linear, two-dimensional analysis which is decoupled from the nonlinear, one-dimensional global analysis for the beam. In this study, a composite cross section analysis model, developed by Kosmatka[26] is used to calculate the shear center location and the modulus weighted section constants of an arbitrarily shaped composite cross section. This model is based on the Saint Venant solution of a tip loaded composite cantilever beam with a general prismatic cross section. It uses the principle of minimum potential energy and 2-D finite element analysis to calculate the cross-sectional warping functions and stress distribution. The shear center location is determined using moment equilibrium and the shear stress distribution. Several other two-dimensional composite cross section analysis models are also available in the literature[27-30], among which Reference 28, which is also capable of modeling cross sections with arbitrary shape and anisotropic and nonhomogeneous materials, is the most general model.

2.4.2 Kinetic Energy

The variation of the kinetic energy for each beam element is

$$\delta T = \int_0^{l_e} \iint_A \rho \mathbf{V} \cdot \delta \mathbf{V}\, d\eta d\zeta dx \tag{29}$$

where the velocity vector, $\mathbf{V}$, is obtained by

$$\mathbf{V} = \dot{\mathbf{R}} + \Omega \hat{k}_r \times \mathbf{R} \tag{30}$$

with the position vector, $\mathbf{R}$, of a point P on the deformed beam written in the form

$$\mathbf{R} = c_1 \hat{i}_r + h_c \hat{i}_b + (x + u)\hat{e}_x + v\hat{e}_y + w\hat{e}_z + \eta E_\eta + \zeta E_\zeta + \alpha\Psi \hat{e}_x' \tag{31}$$

All the terms in the expressions of the velocity vector, $\mathbf{V}$, in Eq. (30) were transformed to the $(\hat{e}_x, \hat{e}_y, \hat{e}_z)$ system before carrying out the algebraic manipulations

implied by Eqs. (30) and (29). A transformation between the $(\hat{e}'_x, \hat{e}'_\eta, \hat{e}'_\zeta)$ system and the $(\hat{e}_x, \hat{e}_y, \hat{e}_z)$ system in terms of the displacement variables u, v, w and ϕ is obtained by combining Eqs. (A.4), (A.5) and the trigonometric relations derived from Fig. 6, and applying the ordering scheme

$$\begin{Bmatrix} \hat{e}'_x \\ \hat{e}'_\eta \\ \hat{e}'_\zeta \end{Bmatrix} = [T_{de}] \begin{Bmatrix} \hat{e}_x \\ \hat{e}_y \\ \hat{e}_z \end{Bmatrix} \tag{32}$$

where the transformation matrix $[T_{de}]$ is expressed as

$$[T_{de}] = [T_{dc}][T_{ce}]$$

$$= \begin{bmatrix} 1 & v_{,x} & w_{,x} \\ -v_{,x}c\beta\phi - w_{,x}s\beta\phi & c\beta\phi & s\beta\phi \\ v_{,x}s\beta\phi - w_{,x}c\beta\phi & -s\beta\phi + \tau_c' c\beta & c\beta\phi + \tau_c' s\beta \end{bmatrix} \tag{33}$$

where

$$\tau_c' = (v_{,x}\sin\beta - w_{,x}\cos\beta)(v_{,x}\cos\beta + w_{,x}\sin\beta)$$

and the notations $c\beta\phi$, $s\beta\phi$, $c\beta$ and $s\beta$ used in Eq. 33 are defined as

$$c\beta\phi \equiv \cos(\beta + \phi), \quad c\beta \equiv \cos\beta$$

$$s\beta\phi \equiv \sin(\beta + \phi), \quad s\beta \equiv \sin\beta$$

Integrating Eq. (29) over the cross section yields mass weighted section constants about the shear center, which are also presented in Appendix B.

2.4.3 External Work Contributions

The effects of the nonconservative distributed loads are included using the principle of virtual work. The virtual work done on each beam element is

$$\delta W_e = \int_0^{l_e} (\mathbf{P}\cdot\delta\mathbf{u} + \mathbf{Q}\cdot\delta\vec{\Theta})\,dx \tag{34}$$

where **P** and **Q** are the distributed force and moment vectors, respectively, along the elastic axis; $\delta\mathbf{u}$ and $\delta\vec{\Theta}$ are the virtual displacement and virtual rotation vectors, respectively, of a point on the deformed elastic axis. In the aeroelastic analysis, components of **P** and **Q** are replaced by the corresponding components of aerodynamic forces and moments.

3. Method of Solution

3.1 Finite Element Discretization

The blade is divided into a series of beam elements. For a swept-tip blade, a single beam element is used to model the tip. The discretized form of Hamilton's principle is written as

$$\int_{t_1}^{t_2} \sum_{i=1}^{n} (\delta U_i - \delta T_i - \delta W_{ei})\, dt = 0 \tag{35}$$

where n is the total number of finite elements. Hermite interpolation polynomials are used to discretize the space dependence: cubic polynomials for v and w; quadratic polynomials for ϕ, u, α, $\bar{\gamma}_{x\eta}$, $\bar{\gamma}_{x\zeta}$. Each beam element consists of two end nodes and one internal node at its mid-point, resulting in a total of 23 nodal degrees of freedom, as shown in Fig. 7. The quadratic polynomial has the capability of modeling a linear variation of strains along the element length, thus being compatible with the cubic polynomial for transverse deflections. These polynomials also satisfy all inter-element compatibility requirements associated with the variational principle in this formulation. Note that when the problem is restricted to bending and shear in the vertical plane, Eqs. (24a-c) reduce to the strain-displacement relations of Timoshenko beam where a constraint relation, such as

$$w_{,x} = \theta_w + \bar{\gamma}_{x\zeta} \tag{36}$$

exists, and θ_w is the rotation due to bending. In this special case the boundary terms for $\delta w_{,x}$ and $\delta\bar{\gamma}_{x\zeta}$ in the δU expression will have the same coefficient with opposite sign, and thus can be combined into a boundary term containing only $\delta\theta_w$. This also agrees with Timoshenko beam theory and implies that $w_{,x}$ and $\bar{\gamma}_{x\zeta}$ are not required to have inter-element continuity[31] . For a beam with built-in twist, undergoing moderate deflections in two mutually perpendicular planes, combined with torsion and transverse shears, the boundary terms for $\delta w_{,x}$ and $\delta\bar{\gamma}_{x\zeta}$ have different coefficients which contain coupling terms such as $v_{,x}$, ϕ and β, and Eq. (36) is no longer valid. The corresponding variational principle thus requires inter-element continuity on both $w_{,x}$ and $\bar{\gamma}_{x\zeta}$, and for the same reason also on $v_{,x}$ and $\bar{\gamma}_{x\eta}$. In the literature of Timoshenko beam finite elements, there is a group of higher order elements[32-34] which also enforced inter-element continuity on $w_{,x}$ and $\bar{\gamma}_{x\zeta}$ either directly or indirectly through Eq. (36); and they produced excellent agreement with exact solutions. For more complex structures such as swept-tip blades, the actual behavior of $\bar{\gamma}_{x\eta}$ and $\bar{\gamma}_{x\zeta}$ at the junction of the swept tip and the straight portion of the blade is complicated. Therefore, the enforcement of inter-element continuity on $\bar{\gamma}_{x\eta}$ and $\bar{\gamma}_{x\zeta}$ at the junction node should be treated as an assumption.

The local-to-global coordinate transformation for the swept-tip element can be written in the form

$$q_t^L = [\Lambda]\, q_t^G \tag{37}$$

where the subscript t denotes quantities associated with the tip element; the superscripts L and G denote the local and global coordinate system, respectively; **q** is the vector of element nodal degrees of freedom, defined as

$$q = [\{v\}^T, \{w\}^T, \{\phi\}^T, \{u\}^T, \{\alpha\}^T, \{\bar{\gamma}_{x\eta}\}^T, \{\bar{\gamma}_{x\zeta}\}^T]^T \tag{38}$$

where $\{v\},\{w\},\{\phi\},\{u\},\{\alpha\},\{\bar{\gamma}_{x\eta}\}$ and $\{\bar{\gamma}_{x\zeta}\}$ are arrays of time dependent nodal values for $v, w, \phi, u, \alpha, \bar{\gamma}_{x\eta}$ and $\bar{\gamma}_{x\zeta}$, respectively. The transformation matrix, $[\Lambda]$, is derived with the constraint that the angular relationship between the swept-tip and the straight portion of the blade at the junction is preserved after deformation[22] . As a result, the transformation corresponding to the rotational degrees of freedom of the junction node is nonlinear due to moderate rotation.

3.2 Solution Procedure for Hover

The first step in the solution procedure is the calculation of the natural frequencies and mode shapes of the blade; which is assumed to be represented by the linear, undamped equations of motion of the blade in vacuum. A modal coordinate transformation is then performed to reduce the number of degrees of freedom of the problem and to assemble the various element matrices into the system mass, damping and stiffness matrices and into the system load vector. The resulting equations of motion in the modal space are a set of nonlinear, coupled, ordinary differential equations given by

$$[M(y)]\ddot{y} + [C(y)]\dot{y} + [K(y, \dot{y}, \ddot{y})]y + F(y, \dot{y}, \ddot{y}) = 0 \tag{39}$$

The static equilibrium position, y_0, is obtained from Eqs. (39) by setting $\dot{y} = \ddot{y} = 0$ and solving the resulting nonlinear algebraic equations. Subsequently, Eqs. (39) are linearized about the nonlinear static equilibrium position, y_0 , and the stability of the blade is obtained from the solution of a standard eigenvalue problem[20,25] .

4. Results and Discussion

The results of this study are divided into three parts: (1) results illustrating the influence of tip sweep and anhedral for isotropic blades; (2) results for single-cell composite blades emphasizing the influence of ply orientation on aeroelastic stability; and (3) results for two-cell composite blades, emphasizing the influence of ply orientation as well as the combined effect of sweep and ply orientation on aeroelastic stability.

4.1 Effects of Swept Tip

The effects of tip sweep and tip anhedral are presented for a soft-in-plane hingeless blade configuration. The blade is modeled using a total of five finite elements. The swept tip, representing 10% of the blade length, is modeled with one element, while the straight portion is modeled using four elements having equal length. Seven coupled rotating modes, including three flap, two lag, one torsion and one axial mode, are used. The baseline configuration for the straight blade is given in Table 1. The tip sweep angle, Λ_s , is varied between 0° and 40° in increment of 10° each. The tip anhedral angle, Λ_a , is varied between -20° and 20° in increment of 10° each. The thrust coefficient of the rotor, C_T , is maintained at a constant value of 0.005 which is equal to the weight coefficient, C_W , by using a coupled trim-aeroelastic response analysis.

Figures 8 and 9 illustrate the effect of tip sweep on the aeroelastic stability of the blade. Figures 8(a) and 8(b) show the imaginary and real parts, respectively, of the complex eigenvalues for hover as a function of Λ_s , for the baseline configuration. The notation L, F and T is used to denote lag, flap and torsion modes,

respectively. The imaginary part of the eigenvalue represents the frequency while the real part of the eigenvalue represents damping of the mode. Tip sweep introduces flap-torsion coupling in the blade. However, for this baseline configuration, the frequencies of the flap and torsion modes are well separated, therefore varying the tip sweep angle does not have a significant influence on the blade stability. Figure 8(a) shows that the frequencies of the first five modes are insensitive to Λ_s while the frequency of the third flap mode increases slightly with Λ_s. The damping in the first flap, first lag and first torsion modes decrease slightly with Λ_s, but no instability is induced by tip sweep, as shown in Fig. 8(b). Figures 9(a) and 9(b) show the imaginary and real parts, respectively, of the eigenvalues as a function of Λ_s, for a configuration with a torsional frequency of $\omega_{T1} = 3.263$/rev which is close to the second flap frequency of $\omega_{F2} = 3.406$/rev. Figure 9(a) shows that frequency coalescence has occurred between the first torsion and second flap modes over a large portion of the tip sweep range being investigated (approximately between 5° and 30°). The effect of this frequency coalescence on the stability is evident in Figure 9(b) where one of the modes is stabilized while the other mode is destabilized. The second flap mode becomes unstable for Λ_s between 10° and 32°. The second lag mode also exhibits a slight instability. This instability is not associated with frequency coalescence and can be removed by a small amount of structural damping.

Figures 10 and 11 illustrate the effect of tip anhedral on the aeroelastic stability of the blade. Figures 10(a) and 10(b) show the imaginary and real parts, respectively, of the eigenvalues for hover as a function of the anhedral angle, Λ_a, for the baseline configuration. Tip anhedral introduces lag-torsion coupling in the blade. The frequencies of the first torsion and second lag modes for the baseline configuration are $\omega_{T1} = 4.875$/rev and $\omega_{L2} = 4.465$/rev, respectively, which are reasonably separated from each other. These two modes exhibit a mild frequency coalescence near $\Lambda_a = 0$ in Fig. 10(a). This frequency coalescence has some destabilizing effect on the first torsion mode when $\Lambda_a > 0°$ or $\Lambda_a < -10°$ and some stabilizing effect on the second lag mode when $\Lambda_a > 0°$, which is evident in Fig. 10(b). Figures 11(a) and 11(b) show the imaginary and real parts, respectively, of the eigenvalues as a function of Λ_a, for a configuration with a torsional frequency of $\omega_{T1} = 4.340$/rev which is close to $\omega_{L2}(= 4.465$/rev). The effect of lag-torsion coupling due to tip anhedral is more pronounced for this blade configuration as Fig. 11(a) exhibits a more apparent frequency coalescence over a wider range, while Fig. 11(b) exhibits a more significant stabilizing effect on the second lag mode and destabilizing effect on the first torsion mode for $\Lambda_a \neq 0°$. The first torsion mode remains stable within the range of anhedral angles considered.

4.2 Single-cell Composite Blade

The behavior of a single-cell composite hingeless blade having a stiff-in-plane blade configuration is considered next. The blade structure is assumed to be represented by a laminated rectangular box beam with uniform spanwise properties, as shown in Figure 12. The cross-section of the beam has an outside dimension of 7″ width by 2″ height with a uniform thickness of 0.35″. The baseline configuration is assumed to have zero ply angles, i.e., all laminates of the beam consists of laminae with fibers parallel to the blade length, and its basic parameters are given in Table 2. Root locus plots are computed for two cases with symmetric configurations where the ply lay-ups on opposite walls are identical. In the first case, the horizontal walls have zero ply angles. For vertical walls the laminae in the outer half thickness have zero ply angles while the laminae in the inner half thickness are all oriented at the same ply angle Λ_v. A positive Λ_v implies that

fibers are oriented toward the top wall of the blade. In the second case, the vertical walls have zero ply angles. For horizontal walls the laminae in the outer half thickness have zero ply angles while the laminae in the inner half thickness are all oriented at the same ply angle Λ_h . A positive Λ_h implies that fibers are oriented toward the leading edge of the blade.

Figures 13 through 15 show the root locus plots of the complex eigenvalues as a function of Λ_v for first lag, first flap and first torsion modes, respectively, at thrust levels $C_T = 0.005$ (solid lines) and $C_T = 0.0025$ (dotted lines). The ply angle Λ_v , which is the parameter given on the plots, is varied from 0° to 90° in both positive and negative directions. Note that the ply angles Λ_v for 90° and -90° have the same configuration with fibers oriented vertically, perpendicular to the blade axis, for the inner half of the vertical walls. The variation of Λ_v influences the direct stiffness terms and the coupling terms which represent the effects of lag-torsion, lag-warp and warp-torsion couplings. Figure 13 shows that a positive ply angle Λ_v destabilizes the first lag mode, while a negative Λ_v stabilizes the first lag mode. Since the first lag mode is not heavily damped, the destabilizing effect on this mode due to positive Λ_v can be significant for certain ply angles. The combined effect of having a positive ply angle Λ_v between 10° and 28° with a low thrust level $C_T = 0.0025$ causes instability in the first lag mode, as illustrated in Fig. 13. Figure 14 shows that a positive Λ_v , up to approximately 45°, stabilizes the first flap mode. A positive Λ_v greater than 45° or a negative Λ_v, on the other hand, destabilizes the first flap mode. For the first torsion mode, varying Λ_v has little influence on its stability, as can be seen in Figure 15. Since the flap and torsion modes are heavily damped, the effect of Λ_v on the stability of these two modes is less significant.

Figures 16 through 18 show the root locus plots of the eigenvalues as a function of Λ_h for the first lag, first flap and first torsion modes, respectively, at a constant thrust coefficient $C_T = 0.005$. Figure 16 shows that a negative Λ_h, up to approximately -60°, destabilizes the first lag mode, while a negative Λ_h beyond -60° or a positive Λ_h stabilizes the first lag mode. For the first flap and first torsion modes, the variation of ply angle Λ_h has a more significant influence on the frequency than on the stability, as illustrated in Figs. 17 and 18.

4.3 Two-cell Composite Blade

Results illustrating the aeroelastic behavior of a composite soft-in-plane blade having a two-cell type cross section are presented next. The two-cell cross-section was selected such that its fundamental natural frequencies for the baseline configuration are similar to those associated with a typical helicopter blade. Figure 19 shows the two-dimensional finite element model employed for the composite cross-section analysis from which the cross-sectional properties of the two-cell type of cross-section were obtained. The leading edge has a semi-circular shape with a radius of 1.2″ ; and the straight portion has a total length of 6″. The middle wall is 2.8″ behind the leading edge semi-circle. All of the walls have a thickness of 0.1″. The baseline configuration of this blade is shown in Table 3 where the material constants correspond to glass/epoxy type composite material. For convenience, it is assumed that the blade has uniform spanwise properties, however, the analysis developed can represent blades with arbitrary mass and stiffness variation. Stability results are first calculated for a swept-tip blade with zero ply angles and for a straight blade with ply angle variation in either the vertical walls or the horizontal walls. The combined effects of tip sweep and ply orientation on blade stability are then calculated. The thrust coefficient C_T is maintained at a constant value of 0.005 for all cases.

Figures 20(a) and 20(b) illustrate the behavior of the imaginary and real parts, respectively, of the eigenvalues associated with the various modes used in the analysis as a function of the tip sweep angle Λ_s, for the baseline configuration which has zero ply angles. For this case, the blade exhibits a frequency coalescence induced by sweep between the second flap and first torsion modes which is evident in Figure 20(a). This produces a stabilizing effect on the second flap mode while destabilizing the first torsion mode, as evident from Figure 20(b). Figure 20(b) shows that the frequency coalescence for this two-cell case induces a mild instability in the first torsion mode for sweep angles between 15° and 20°.

For the straight blade with ply angle variations, two cases are analyzed. In the first case, the laminae in the middle vertical wall and the inner half of the rear vertical wall are oriented at ply angle Λ_v while the remaining walls have zero ply angles. In the second case, the laminae in the inner half of the horizontal walls are oriented at ply angle Λ_h while the remaining walls have zero ply angles. Figures 21 through 23 show the root-locus plots of the eigenvalues as a function of the ply angle Λ_v for first lag, first flap and first torsion modes, respectively. Figure 21 shows that a positive Λ_v, or a negative Λ_v beyond -40°, destabilizes the first lag mode, while a negative Λ_v up to -40° stabilizes the mode. The effects of the ply angle Λ_v variation on the first flap and first torsion modes are less significant, as illustrated in Figs. 22 and 23.

Figures 24 through 27 show the root locus plots of the eigenvalues as a function of the ply angle Λ_h for the first lag, first flap, first torsion and second flap modes, respectively, for the straight blade case (solid lines) and for the swept tip case with $\Lambda_s = 20°$ (dotted lines). Figure 24 shows that a positive Λ_h or a negative Λ_h beyond -40° destabilizes the first lag mode, while a negative Λ_h up to -40° stabilizes the mode. The first flap mode stability is only slightly influenced by the variation of Λ_h, as illustrated in Fig. 25. The 20° tip sweep has a destabilizing effect on both the first lag and first flap modes, but no instability is induced in these modes, as shown in Figs. 24 and 25. Figure 26 shows that for the straight blade case, the damping in the first torsion mode decreases for positive Λ_h, however, the mode remains stable. For the case of 20° sweep, the blade has a mild instability in the first torsion mode at zero ply angle, which has been shown in Fig. 20(b). The first torsion mode is further destabilized for ply angle Λ_h between 0° and 12°, however, it becomes stable for Λ_h greater than 12° or for a negative ply angle Λ_h, as illustrated in Fig. 26. Therefore, it is possible to remove the instability due to tip sweep by choosing the appropriate ply orientation in the composite blades. The effect of the 20° sweep, compared to the straight blade case, is to destabilize the first torsion mode and stabilize the second flap mode for all ply angles, as shown in Figs. 26 and 27, respectively.

5. Concluding Remarks

An analytical study of the aeroelastic behavior of composite rotor blades with straight and swept tips, based on a new aeroelastic model, has been presented. The new aeroelastic model is based upon Hamilton's principle and employs a finite element formulation. Numerical results showing the effects of tip sweep and anhedral, and composite ply orientation on the aeroelastic stability of the blade in hover are presented so as to illustrate the potential of the model for aeroelastic tailoring and structural optimization studies. The main conclusions obtained are summarized below:

(1) It is essential to use a coupled trim-aeroelastic response analysis for swept-tip blades so that a constant thrust coefficient can be appropriately maintained throughout the range of tip sweep and tip anhedral variation.

(2) Tip sweep can cause aeroelastic instability due to frequency coalescence between the first torsion and second flap modes.

(3) When frequency coalescence occurs between the first torsion and second lag modes, both tip anhedral and dihedral have a stabilizing effect on the second lag mode.

(4) Ply angle variation in composite blades has a significant influence on the stability of the first lag mode. The combined effect of low thrust condition and certain ply orientations can cause blade instability in the first lag mode.

(5) The aeroelastic instability induced by tip sweep can be removed by appropriate modification of the torsional stiffness of the blade. For composite blades, proper choice of ply orientation can be used as an additional design variable which will remove this instability.

(6) Blade sweep, anhedral and coupling introduced by the composite construction of the blade are important design parameters which can be exploited in the aeroelastic tailoring and structural optimization studies of advanced rotor blades.

Acknowledgements

This research was supported by NASA Langley Research center under grant NAG-1-833, with Dr. H. Adelman as grant monitor. The authors wish to express their gratitude to Professor J. Kosmatka from AMES Department of the University of California, San Diego, for providing the authors with a copy of his computer code which was used to calculate the shear center location and the modulus weighted section constants.

Appendix A

Transformation Matrices Between Coordinate Systems

$$\begin{Bmatrix} \hat{i}_r \\ \hat{j}_r \\ \hat{k}_r \end{Bmatrix} = [\,T_m\,] \begin{Bmatrix} \hat{i}_{nr} \\ \hat{j}_{nr} \\ \hat{k}_{nr} \end{Bmatrix} \tag{A.1a}$$

where

$$[\,T_m\,] = \begin{bmatrix} \cos\psi & \sin\psi & 0 \\ -\sin\psi & \cos\psi & 0 \\ 0 & 0 & 1 \end{bmatrix} \tag{A.1b}$$

$$\begin{Bmatrix} \hat{i}_b \\ \hat{j}_b \\ \hat{k}_b \end{Bmatrix} = [\,T_{br}\,] \begin{Bmatrix} \hat{i}_r \\ \hat{j}_r \\ \hat{k}_r \end{Bmatrix} \tag{A.2a}$$

where

$$[T_{br}] = \begin{bmatrix} 1 & 0 & 0 \\ 0 & \cos\theta_p & \sin\theta_p \\ 0 & -\sin\theta_p & \cos\theta_p \end{bmatrix} \begin{bmatrix} \cos\beta_p & 0 & \sin\beta_p \\ 0 & 1 & 0 \\ -\sin\beta_p & 0 & \cos\beta_p \end{bmatrix} \tag{A.2b}$$

$$\begin{Bmatrix} \hat{c}_x \\ \hat{c}_y \\ \hat{c}_z \end{Bmatrix} = [T_{cb}] \begin{Bmatrix} \hat{i}_b \\ \hat{j}_b \\ \hat{k}_b \end{Bmatrix} \tag{A.3a}$$

For the straight portion of the blade:

$$[T_{cb}] = \begin{bmatrix} 1 & 0 & 0 \\ 0 & 1 & 0 \\ 0 & 0 & 1 \end{bmatrix} \tag{A.3b}$$

For the swept-tip:

$$[T_{cb}] = \begin{bmatrix} \cos\Lambda_s & -\sin\Lambda_s & 0 \\ \sin\Lambda_s & \cos\Lambda_s & 0 \\ 0 & 0 & 1 \end{bmatrix} \begin{bmatrix} \cos\Lambda_a & 0 & \sin\Lambda_a \\ 0 & 1 & 0 \\ -\sin\Lambda_a & 0 & \cos\Lambda_a \end{bmatrix} \tag{A.3c}$$

$$\begin{Bmatrix} \hat{e}_x \\ \hat{e}_\eta \\ \hat{e}_\zeta \end{Bmatrix} = [T_{ce}] \begin{Bmatrix} \hat{e}_x \\ \hat{e}_y \\ \hat{e}_z \end{Bmatrix} \tag{A.4a}$$

where

$$[T_{ce}] = \begin{bmatrix} 1 & 0 & 0 \\ 0 & \cos\beta & \sin\beta \\ 0 & -\sin\beta & \cos\beta \end{bmatrix} \tag{A.4b}$$

$$\begin{Bmatrix} \hat{e}'_x \\ \hat{e}'_\eta \\ \hat{e}'_\zeta \end{Bmatrix} = [T_{dc}] \begin{Bmatrix} \hat{e}_x \\ \hat{e}_\eta \\ \hat{e}_\zeta \end{Bmatrix} \tag{A.5a}$$

where

$[T_{dc}] =$

$$\begin{bmatrix} 1 & 0 & 0 \\ 0 & \cos\theta_x & \sin\theta_x \\ 0 & -\sin\theta_x & \cos\theta_x \end{bmatrix} \begin{bmatrix} \cos\theta_\eta & 0 & -\sin\theta_\eta \\ 0 & 1 & 0 \\ \sin\theta_\eta & 0 & \cos\theta_\eta \end{bmatrix} \begin{bmatrix} \cos\theta_\zeta & \sin\theta_\zeta & 0 \\ -\sin\theta_\zeta & \cos\theta_\zeta & 0 \\ 0 & 0 & 1 \end{bmatrix} \tag{A.5b}$$

Appendix B

Modulus Weighted and Mass Weighted Section Constants

(1) Modulus weighted area, first and second moments of inertia, and torsional integrals:

$$EA = \iint_{\Lambda} Q_{11}\, d\eta d\zeta$$

$$EA\eta_a = \iint_{\Lambda} Q_{11}\, \eta\, d\eta d\zeta$$

$$EA\zeta_a = \iint_{\Lambda} Q_{11}\, \zeta\, d\eta d\zeta$$

$$EI_{\eta\eta} = \iint_{A} Q_{11}\, \zeta^2\, d\eta d\zeta$$

$$EI_{\zeta\zeta} = \iint_{A} Q_{11}\, \eta^2\, d\eta d\zeta$$

$$EI_{\eta\zeta} = \iint_{\Lambda} Q_{11}\, \eta\zeta\, d\eta d\zeta$$

$$EAC_0 = \iint_{\Lambda} Q_{11}\, (\eta^2 + \zeta^2)\, d\eta d\zeta$$

$$EAC_1 = \iint_{\Lambda} Q_{11}\, \eta\, (\eta^2 + \zeta^2)\, d\eta d\zeta$$

$$EAC_2 = \iint_{\Lambda} Q_{11}\, \zeta\, (\eta^2 + \zeta^2)\, d\eta d\zeta$$

$$EAC_3 = \iint_{\Lambda} Q_{11}\, (\eta^2 + \zeta^2)^2\, d\eta d\zeta$$

$$G_\eta A = \iint_\Lambda Q_{16}\, d\eta d\zeta$$

$$G_\zeta A = \iint_\Lambda Q_{15}\, d\eta d\zeta$$

$$G_{\eta\eta} A = \iint_\Lambda Q_{66}\, d\eta d\zeta$$

$$G_{\zeta\zeta} A = \iint_\Lambda Q_{55}\, d\eta d\zeta$$

$$G_{\eta\zeta} A = \iint_\Lambda Q_{56}\, d\eta d\zeta$$

$$G_\eta A\eta_b = \iint_\Lambda Q_{16}\, \eta\, d\eta d\zeta$$

$$G_\eta A\zeta_b = \iint_\Lambda Q_{16}\, \zeta\, d\eta d\zeta$$

$$G_\zeta A\eta_c = \iint_\Lambda Q_{15}\, \eta\, d\eta d\zeta$$

$$G_\zeta A\zeta_c = \iint_\Lambda Q_{15}\, \zeta\, d\eta d\zeta$$

$$G_\eta J = \iint_\Lambda Q_{16}\, (\eta^2 + \zeta^2)\, d\eta d\zeta$$

$$G_\zeta J = \iint_\Lambda Q_{15}\, (\eta^2 + \zeta^2)\, d\eta d\zeta$$

$$GJ = \iint_\Lambda (Q_{55}\, \eta^2 + Q_{66}\, \zeta^2 - 2Q_{56}\, \eta\zeta)\, d\eta d\zeta$$

(2) Modulus weighted area, first and second moment warping integrals:

$$EAD_0 = \iint_\Lambda Q_{11}\,\Psi\,d\eta d\zeta$$

$$EAD_1 = \iint_\Lambda Q_{11}\,\eta\Psi\,d\eta d\zeta$$

$$EAD_2 = \iint_\Lambda Q_{11}\,\zeta\Psi\,d\eta d\zeta$$

$$EAD_3 = \iint_\Lambda Q_{11}\,\Psi^2\,d\eta d\zeta$$

$$EAD_4 = \iint_\Lambda Q_{11}\,(\eta^2+\zeta^2)\,\Psi\,d\eta d\zeta$$

$$EAD_5 = \iint_\Lambda Q_{11}\,\tau_0\,\Psi\,(\zeta\Psi_{,\eta} - \eta\Psi_{,\zeta})\,d\eta d\zeta$$

$$EAD_6 = \iint_\Lambda Q_{15}\,\Psi\,d\eta d\zeta$$

$$EAD_7 = \iint_\Lambda Q_{16}\,\Psi\,d\eta d\zeta$$

$$EAD_0' = \iint_\Lambda Q_{11}\,\tau_0\,(\zeta\Psi_{,\eta} - \eta\Psi_{,\zeta})\,d\eta d\zeta$$

$$EAD_1' = \iint_\Lambda Q_{11}\,\tau_0\,\eta\,(\zeta\Psi_{,\eta} - \eta\Psi_{,\zeta})\,d\eta d\zeta$$

$$EAD_2' = \iint_\Lambda Q_{11}\,\tau_0\,\zeta\,(\zeta\Psi_{,\eta} - \eta\Psi_{,\zeta})\,d\eta d\zeta$$

$$EAD_3' = \iint_\Lambda Q_{11}\,\tau_0^2\,(\zeta\Psi_{,\eta} - \eta\Psi_{,\zeta})^2\,d\eta d\zeta$$

$$EAD_4' = \iint_\Lambda Q_{11}\tau_0(\eta^2+\zeta^2)(\zeta\Psi_{,\eta}-\eta\Psi_{,\zeta})\,d\eta d\zeta$$

$$EAD_6' = \iint_\Lambda Q_{15}\tau_0(\zeta\Psi_{,\eta}-\eta\Psi_{,\zeta})\,d\eta d\zeta$$

$$EAD_7' = \iint_\Lambda Q_{16}\tau_0(\zeta\Psi_{,\eta}-\eta\Psi_{,\zeta})\,d\eta d\zeta$$

(3) Anisotropic material stiffness coupling integrals:

$$EAB_0 = \iint_\Lambda (Q_{15}\eta - Q_{16}\zeta)\,d\eta d\zeta$$

$$EAB_1 = \iint_\Lambda (Q_{15}\eta - Q_{16}\zeta)\eta\,d\eta d\zeta$$

$$EAB_2 = \iint_\Lambda (Q_{15}\eta - Q_{16}\zeta)\zeta\,d\eta d\zeta$$

$$EAB_3 = \iint_\Lambda (Q_{15}\eta - Q_{16}\zeta)\Psi\,d\eta d\zeta$$

$$EAB_4 = \iint_\Lambda (Q_{15}\eta - Q_{16}\zeta)(\eta^2+\zeta^2)\,d\eta d\zeta$$

$$EAB_5 = \iint_\Lambda (Q_{15}\Psi_{,\zeta} + Q_{16}\Psi_{,\eta})\,d\eta d\zeta$$

$$EAB_6 = \iint_\Lambda (Q_{15}\Psi_{,\zeta} + Q_{16}\Psi_{,\eta})\eta\,d\eta d\zeta$$

$$EAB_7 = \iint_\Lambda (Q_{15}\Psi_{,\zeta} + Q_{16}\Psi_{,\eta})\zeta\,d\eta d\zeta$$

$$EAB_8 = \iint_\Lambda (Q_{15}\Psi_{,\zeta} + Q_{16}\Psi_{,\eta})\Psi\,d\eta d\zeta$$

$$EAB_9 = \iint_A (Q_{15}\Psi_{,\zeta} + Q_{16}\Psi_{,\eta})(\eta^2 + \zeta^2)\,d\eta d\zeta$$

$$EAB_{10} = \iint_A (Q_{55}\eta - Q_{56}\zeta)\,d\eta d\zeta$$

$$EAB_{11} = \iint_A (Q_{55}\Psi_{,\zeta} + Q_{56}\Psi_{,\eta})\,d\eta d\zeta$$

$$EAB_{12} = \iint_A (Q_{56}\eta - Q_{66}\zeta)\,d\eta d\zeta$$

$$EAB_{13} = \iint_A (Q_{56}\Psi_{,\zeta} + Q_{66}\Psi_{,\eta})\,d\eta d\zeta$$

$$EAB_{14} = \iint_A [(Q_{55}\eta - Q_{56}\zeta)\Psi_{,\zeta} + (Q_{56}\eta - Q_{66}\zeta)\Psi_{,\eta}]d\eta d\zeta$$

$$EAB_{15} = \iint_A [Q_{55}(\Psi_{,\zeta})^2 + Q_{66}(\Psi_{,\eta})^2 + 2Q_{56}\Psi_{,\eta}\Psi_{,\zeta}]d\eta d\zeta$$

$$EAB_3' = \iint_A (Q_{15}\eta - Q_{16}\zeta)(\zeta\Psi_{,\eta} - \eta\Psi_{,\zeta})\,\tau_0\,d\eta d\zeta$$

$$EAB_8' = \iint_A (Q_{15}\Psi_{,\zeta} + Q_{16}\Psi_{,\eta})(\zeta\Psi_{,\eta} - \eta\Psi_{,\zeta})\tau_0\,d\eta d\zeta$$

(4) Mass weighted section constants:

$$m = \iint_A \rho\,d\eta d\zeta$$

$$m\eta_m = \iint_A \rho\eta\,d\eta d\zeta$$

$$m\zeta_m = \iint_A \rho\zeta\,d\eta d\zeta$$

$$Im_{\eta\eta} = \iint_{\Lambda} \rho\zeta^2 \, d\eta d\zeta$$

$$Im_{\zeta\zeta} = \iint_{\Lambda} \rho\eta^2 \, d\eta d\zeta$$

$$Im_{\eta\zeta} = \iint_{\Lambda} \rho\eta\zeta \, d\eta d\zeta$$

$$mD_0 = \iint_{\Lambda} \rho\Psi \, d\eta d\zeta$$

$$mD_1 = \iint_{\Lambda} \rho\Psi\eta \, d\eta d\zeta$$

$$mD_2 = \iint_{\Lambda} \rho\Psi\zeta \, d\eta d\zeta$$

$$mD_3 = \iint_{\Lambda} \rho\Psi^2 \, d\eta d\zeta$$

References

1. Hodges, D.H. and Dowell, E.H., "Nonlinear Equations of Motion for the Elastic Bending and Torsion of Twisted Nonuniform Rotor Blades," NASA TN D-7818, December 1974.

2. Hodges, D.H. and Ormiston, R.A., "Stability of Elastic Bending and Torsion of Uniform Cantilever Rotor Blades in Hover with Variable Structural Coupling," NASA TN D-8192, 1976.

3. Rosen, A., and Friedmann, P.P., "Nonlinear Equations of Equilibrium for Elastic Helicopter or Wind Turbine Blades Undergoing Moderate Deflection," NASA CR-159478, October 1978.

4. Rosen, A., and Friedmann, P.P., "The Nonlinear Behavior of Elastic Slender Straight Beams Undergoing Small Strains and Moderate Rotations," Journal of Applied Mechanics , vol. 46, March 1979, pp. 161-168.

5. Shamie, J., and Friedmann, P.P., "Effect of Moderate Deflections on the Aeroelastic Stability of a Rotor Blade in Forward Flight," Proceedings of the Third European Rotorcraft and Powered Lift Aircraft Forum ", Aix-en-Provence, 1977, pp. 24.1-24.37.

6. Kaza, K.R. and Kvaternik, R.G., "Nonlinear Aeroelastic Equations for Combined Flapwise Bending, Chordwise Bending, Torsion and Extension of Twisted Non-Uniform Rotor Blades in Forward Flight," NASA TM-74059, 1977.

7. Hodges, D.H., "Nonlinear Equations for Dynamics of Pretwisted Beams Undergoing Small Strains and Large Rotations," NASA TP-2470, May 1985.

8. Friedmann, P.P., "Helicopter Rotor Dynamics and Aeroelasticity: Some Key Ideas and Insights," Vertica , vol.14, No. 1, 1990, pp. 101-121.

9. Hodges, D.H., "Review of Composite Rotor Blade Modeling," AIAA Journal , Vol 28, No. 3, 1990, pp. 561-565.

10. Hong, C.H., and Chopra, I., "Aeroelastic Stability Analysis of a Composite Rotor Blade," Journal of the American Helicopter Society , Vol. 30, No. 2, 1985, pp. 57-67.

11. Hong, C.H., and Chopra, I., "Aeroelastic Stability of a Composite Bearingless Rotor Blade," Journal of the American Helicopter Society , Vol. 31, No. 4, 1986, pp. 29-35.

12. Panda, B. and Chopra, I., "Dynamics of Composite Rotor Blades in Forward Flight," Vertica , Vol. 11, No. 1/2, 1987, pp. 187-209.

13. Kosmatka, J.B. and Friedmann, P.P., "Vibration Analysis of Composite Turbopropellers Using a Nonlinear Beam-Type Finite Element Approach," AIAA Journal , Vol. 27, No. 11, November 1989, pp. 1606-1614.

14. Bauchau, O.A. and Hong, C.H., "Large Displacement Analysis of Naturally Curved and Twisted Composite Beams," AIAA Journal , Vol. 25, No. 11, November 1987, pp. 1469-1475.

15. Bauchau, O.A. and Hong, C.H., "Nonlinear composite Beam Theory," Journal of Applied Mechanics , Vol. 55, March 1988, pp. 156-163.

16. Minguet, P. and Dugundji, J., "Experiments and Analysis for Composite Blades Under Large Deflections: Part 1 - Static Behavior," AIAA Journal , Vol. 28, No. 9, September 1990, pp. 1573-1579.

17. Minguet, P. and Dugundji, J., "Experiments and Analysis for Composite Blades Under Large Deflections: Part 2 - Dynamic Behavior," AIAA Journal , Vol. 28, No. 9, September 1990, pp. 1580-1588.

18. Atilgan, A.R. and Hodges, D.H., "A Geometrically Nonlinear Analysis for Nonhomogeneous, Anisotropic Beams," AIAA Paper No. 89-1264-CP, Proc. 30th AIAA/ASME/ASCE/AHS/ACS Structures, Structural Dynamics and Materials Conf., Mobil, AL, April 1989, pp. 895-908.

19. Tarzanin, F.J. Jr., and Vlaminck, R.R., "Investigation of the Effect of Blade Sweep on Rotor Vibratory Loads," NASA CR-166526, October 1983.

20. Celi, R. and Friedmann, P.P., "Aeroelastic Modeling of Swept Tip Rotor Blades Using Finite Elements," Journal of the American Helicopter Society , Vol. 33, No. 2, April 1988, pp. 43-52.

21. Benquet, P. and Chopra, I., "Calculated Dynamic Response and Loads for an Advanced Tip Rotor in Forward Flight," Proceedings of the Fifteenth European Rotorcraft Forum, Amsterdam, Sep. 12-15, 1989.

22. Panda, B., "Technical Note: Assembly of Moderate-Rotation Finite Elements Used in Helicopter Rotor Dynamics," Journal of the American Helicopter Society , Vol. 32, No. 4, 1987, pp. 63-69.

23. Wempner, G., Mechanics of Solids with Application to Thin Bodies Sijthoff & Noordhoff, 1981.

24. Washizu, K., "Some Considerations on a Naturally Curved and Twisted Slender Beam," Journal of Mathematics and Physics , Vol. 43, No. 2, June 1964, pp. 111-116.

25. Celi, R. and Friedmann, P.P., "Rotor Blade Aeroelasticity in Forward Flight with an Implicit Aerodynamic Formulation," AIAA Journal , Vol. 26, No. 12, 1988, pp. 1425-1433.

26. Kosmatka, J.B., "Structural Dynamic Modeling of Advanced Composite Propellers by the Finite Element Method," Ph.D. Dissertation, Mechanical Aerospace and Nuclear Engineering Department, University of California, Los Angeles, 1986.

27. Wörndle, R., "Calculation of the Cross Section Properties and the Shear Stresses of Composite Rotor Blades," Vertica , Vol. 6, 1982, pp. 111-129.

28. Giavotto, V., Borri, M., Mantegazza, P., Ghiringhelli, G., Carmaschi, V., Maffioli, G.C. and Mussi, F., "Anisotropic Beam Theory and Applications," Computers and Structures , Vol. 16, 1983, pp. 403-413.

29. Rehfield, L.W., "Design Analysis Methodology for Composite Rotor Blades," Presented at the 7th DoD/NASA Conf. on Fibrous Composites in Structural Design, Denver, CO, June 17-20, 1985, AFWAL-TR-85-3094, pp. (V(a)-1)-(V(a)-15).

30. Bauchau, O.A., Coffenberry, B.S. and Rehfield, L.W., "Composite Box Beam Analysis: Theory and Experiments," Journal of Reinforced Plastics and composites , Vol. 6, 1987, pp. 25-35.

31. Tessler, A., and Dong, S.B., "On a Hierarchy of Conforming Timoshenko Beam Elements," Computers & Structures , Vol. 14, No. 3-4, 1981, pp. 335-344.

32. Nickell, R.E., and Secor, G.A., "Convergence of Consistently Derived Timoshenko Beam Finite Elements," International Journal for Numerical Methods in Engineering , Vol. 5, 1972, pp. 243-253.

33. Thomas, D.L., Wilson, J.M., and Wilson, R.R., "Timoshenko Beam Finite Elements," Journal of Sound and Vibrations , Vol. 31, 1973, pp. 315-330.

34. Thomas, J., and Abbas, B.A.H., "Finite Element Model for Dynamic Analysis of Timoshenko Beam," Journal of Sound and Vibrations , Vol. 41, 1975, pp. 291-299.

TABLE 1

Baseline configuration for isotropic rotor blade

Fundamental, coupled rotating natural frequencies for a straight blade:

$\omega_{L1} = 0.731$
$\omega_{F1} = 1.125$
$\omega_{T1} = 4.875$

$\gamma = 5.5$	$a = 2\pi$
$\sigma = 0.07$	$C_{d0} = 0.01$
$c/R = 0.055$	$C_W = 0.005$
$\beta_p = 0.0$	$B = 4$

Offsets of center of mass, aerodynamic center and tension center from elastic axis are zero.

Tip length = 10% of the blade length.

TABLE 2

Baseline configuration for single-cell composite rotor blade

Fundamental, coupled rotating natural frequencies for a straight blade with zero ply angles:

$\omega_{L1} = 1.533$
$\omega_{F1} = 1.187$
$\omega_{T1} = 5.186$

$\gamma = 5.0$	$a = 5.7$
$\sigma = 0.1$	$C_{d0} = 0.01$
$c/R = 0.08$	$C_W = 0.005$
$\beta_p = 0.0$	$B = 4$

Offsets of center of mass, aerodynamic center and tension center from elastic axis are zero.

Material constants:

$E_L = 30. \times 10^6$ psi
$E_T = 3. \times 10^6$ psi
$G_{LT} = 1.2 \times 10^6$ psi
$\nu_{LT} = 0.3$

TABLE 3

Baseline configuration for two-cell composite rotor blade

Fundamental, coupled rotating natural frequencies for a straight blade with zero ply angles:

$\omega_{L1} = 0.765$
$\omega_{F1} = 1.096$
$\omega_{T1} = 3.356$

$\gamma = 5.0$	$a = 5.7$
$\sigma = 0.1$	$C_{d0} = 0.01$
$c/R = 0.06$	$C_W = 0.005$
$\beta_p = 0.0$	$B = 4$

Tip length = 10% of the blade length.

Material constants:

$E_L = 6.2 \times 10^6$ psi
$E_T = 1.6 \times 10^6$ psi
$G_{LT} = 0.8 \times 10^6$ psi
$\nu_{LT} = 0.25$

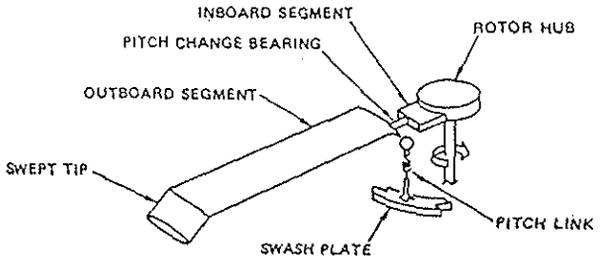

Figure 1: Rotor blade with tip sweep and anhedral

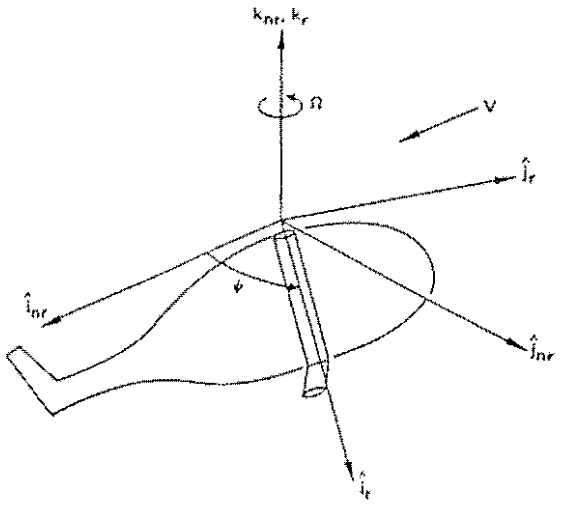

Figure 2: Nonrotating, hub-fixed coordinate system and rotating, hub-fixed coordinate system

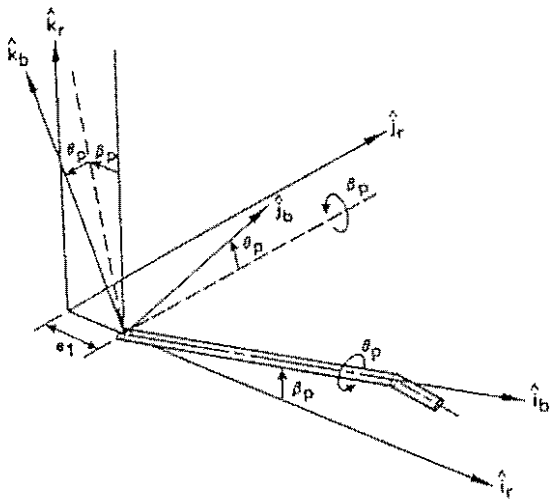

Figure 3: Preconed, pitched, blade-fixed coordinate system

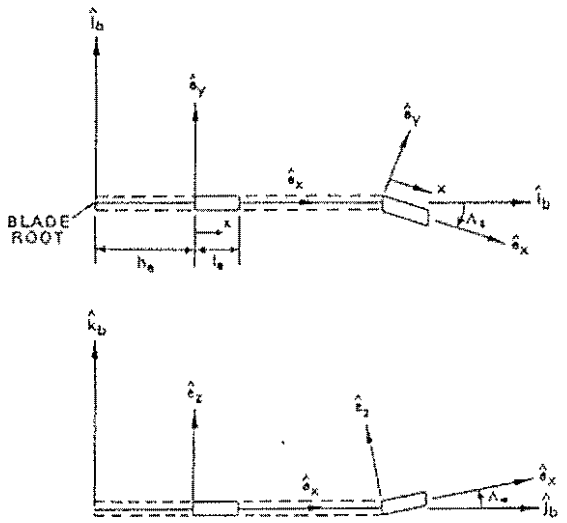

Figure 4: Undeformed element coordinate system

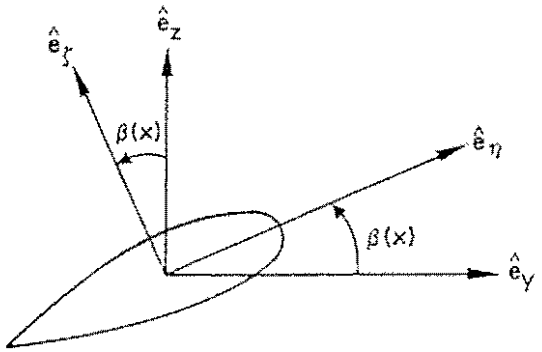

Figure 5: Undeformed curvilinear coordinate system

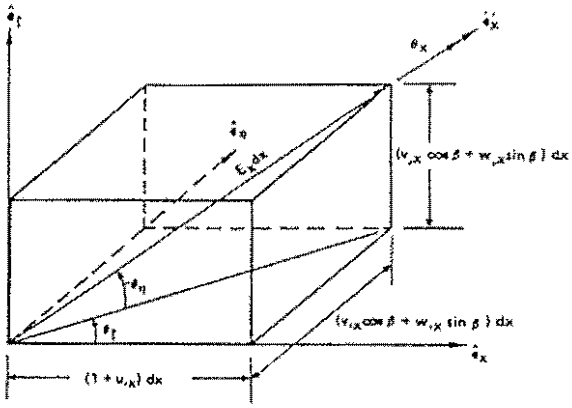

Figure 6: Deformation sequence and Euler angles

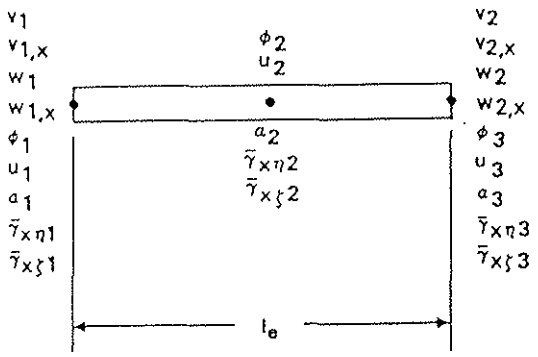

Figure 7: Finite element nodal degrees of freedom

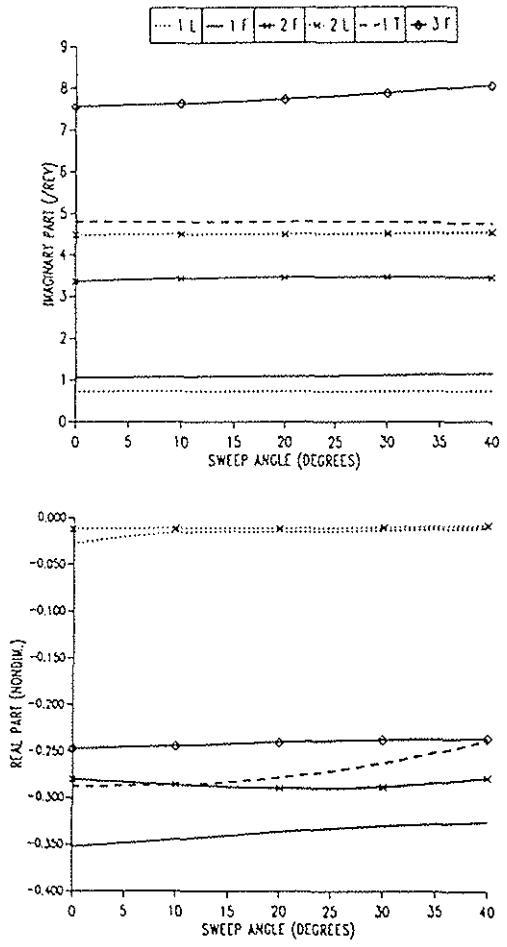

Figure 8: Effect of tip sweep on the aeroelastic stability of the isotropic blade, baseline configuration.
(a) imaginary part of eigenvalues
(b) real part of eigenvalues

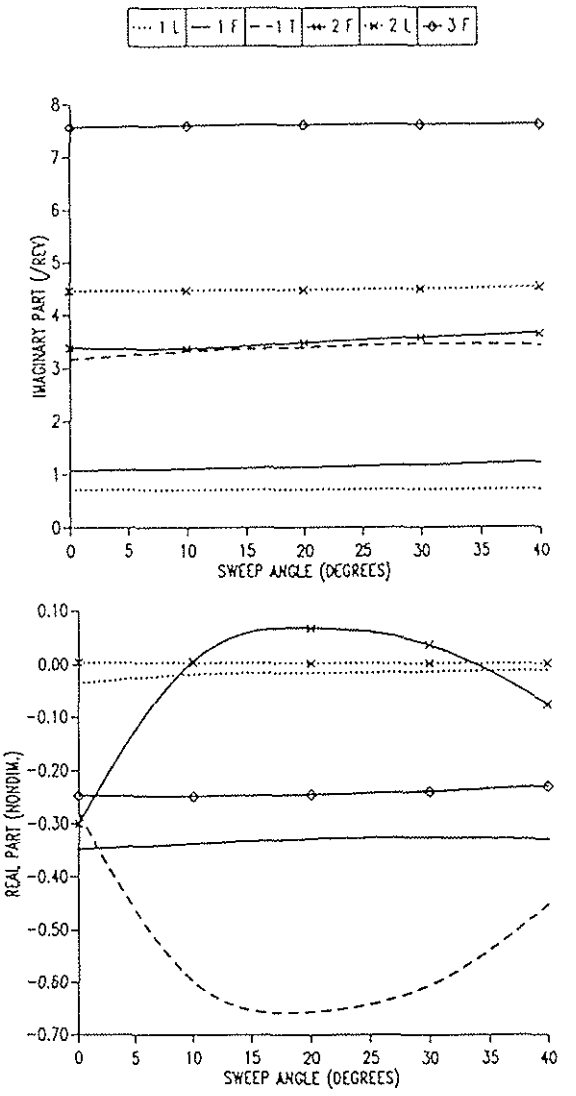

Figure 9: Effect of tip sweep on the aeroelastic stability of the isotropic blade, $\omega_{T1} = 3.263$/rev.
(a) imaginary part of eigenvalues
(b) real part of eigenvalues

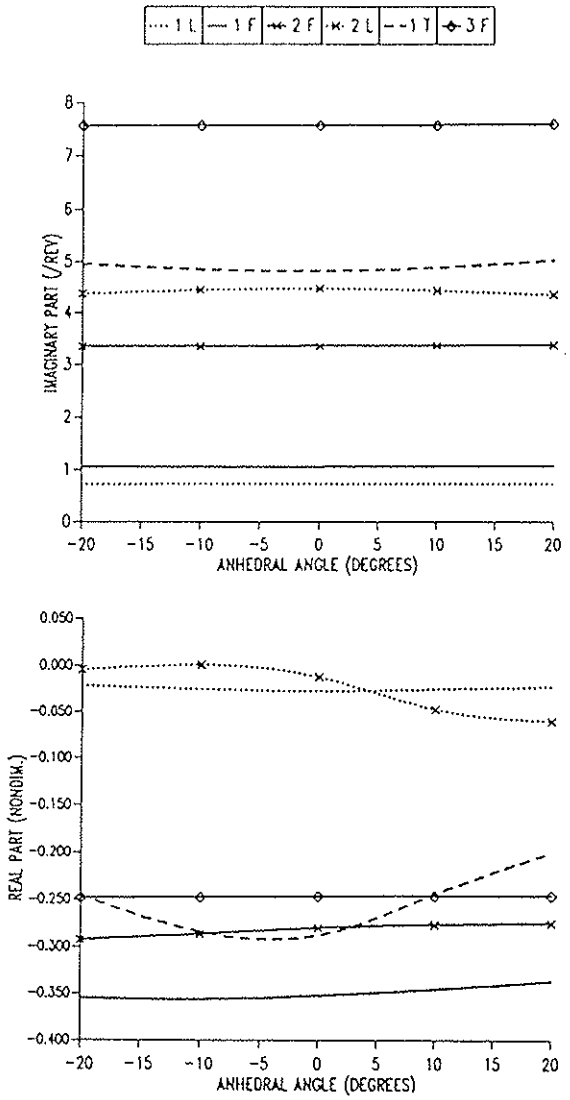

Figure 10: Effect of tip anhedral on the aeroelastic stability of the isotropic blade, baseline configuration.
(a) imaginary part of eigenvalues
(b) real part of eigenvalues

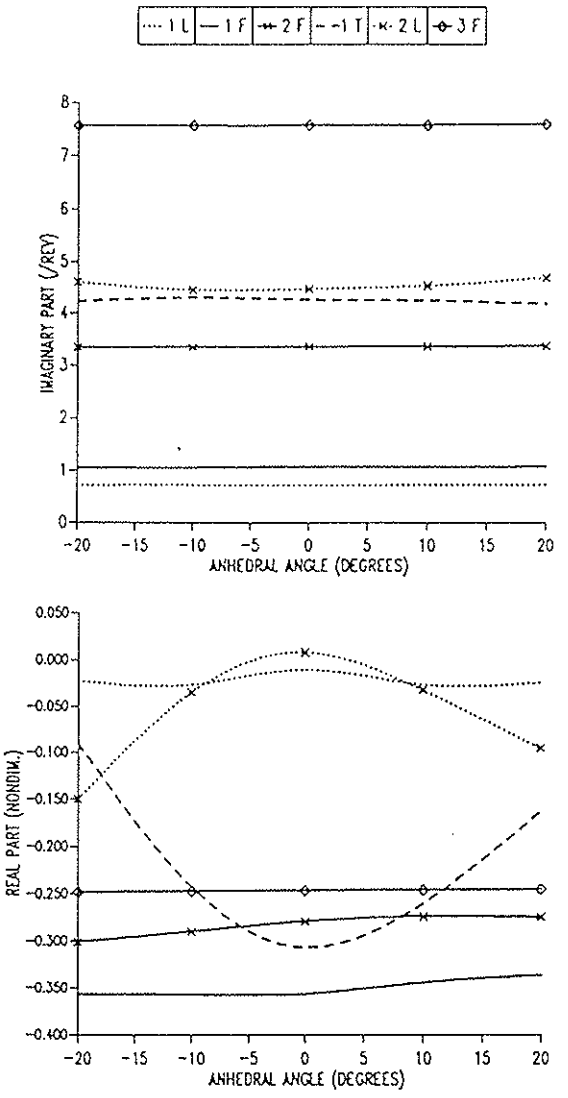

Figure 11: Effect of tip anhedral on the aeroelastic stability of the isotropic blade, $\omega_{T1} = 4.340$/rev.
(a) imaginary part of eigenvalues
(b) real part of eigenvalues

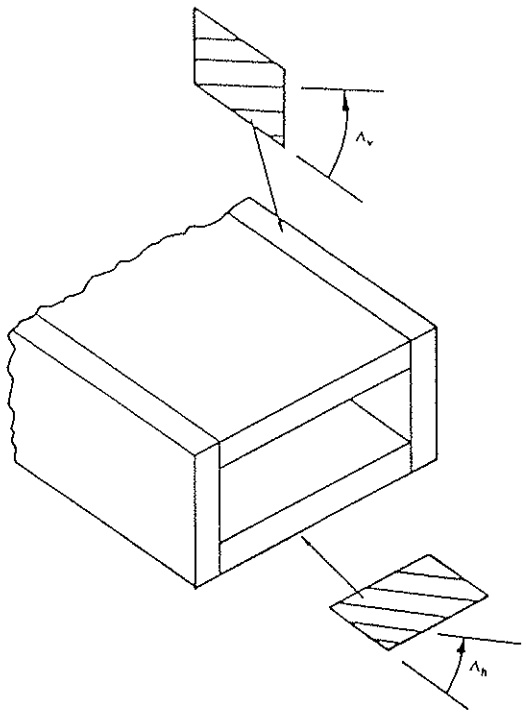

Figure 12: Single-cell laminated rectangular box beam

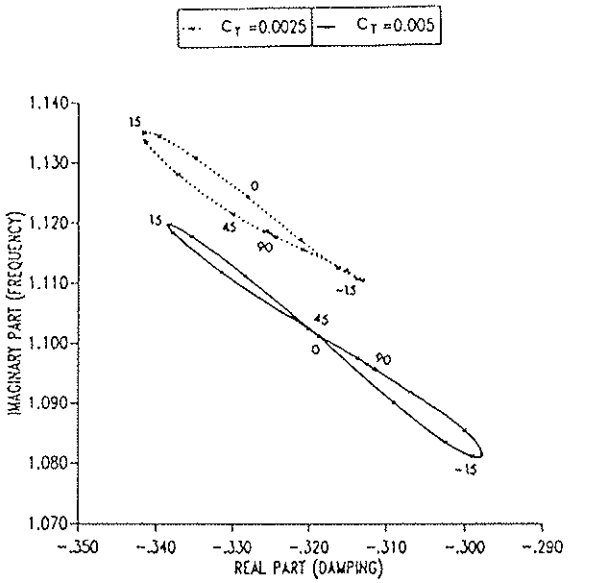

Figure 14: Root locus of first flap eigenvalues as a function of ply angle in vertical wall for single-cell composite blade.

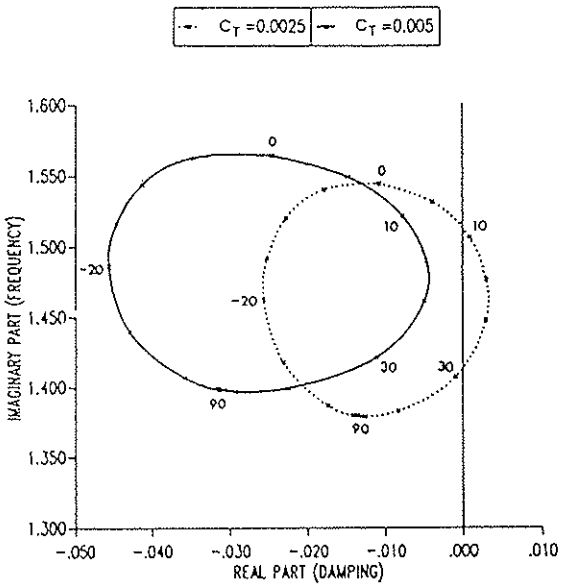

Figure 13: Root locus of first lag eigenvalues as a function of ply angle in vertical wall for single-cell composite blade.

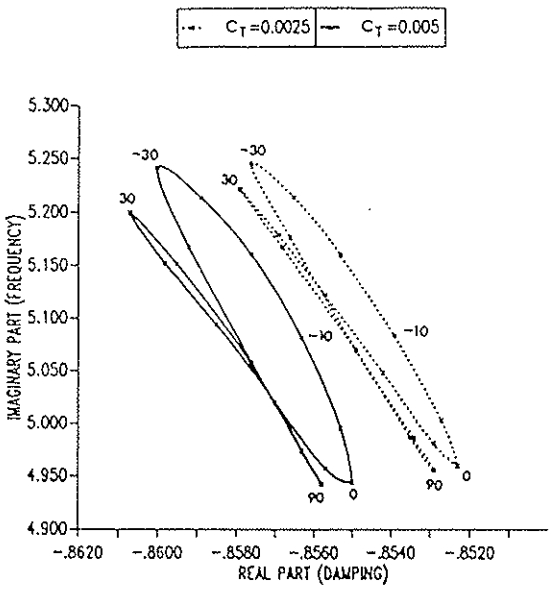

Figure 15: Root locus of first torsion eigenvalues as a function of ply angle in vertical wall for single-cell composite blade.

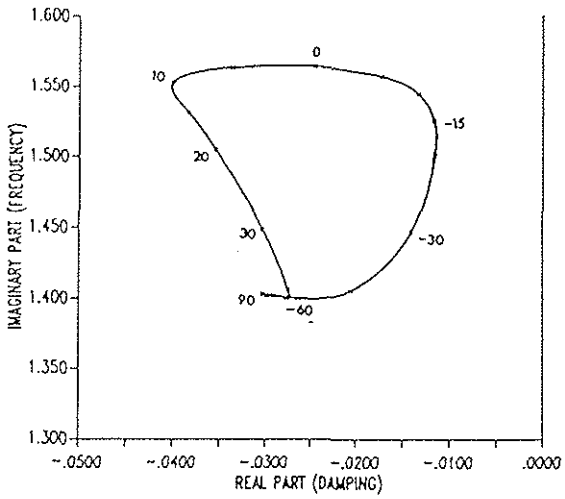

Figure 16: Root locus of first lag eigenvalues as a function of ply angle in horizontal wall for single-cell composite blade.

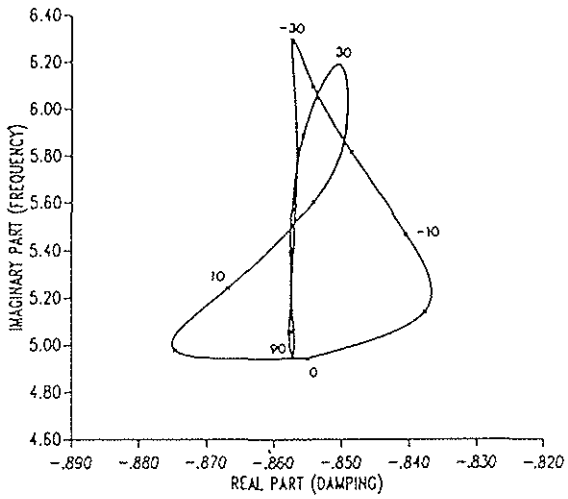

Figure 18: Root locus of first torsion eigenvalues as a function of ply angle in horizontal wall for single-cell composite blade.

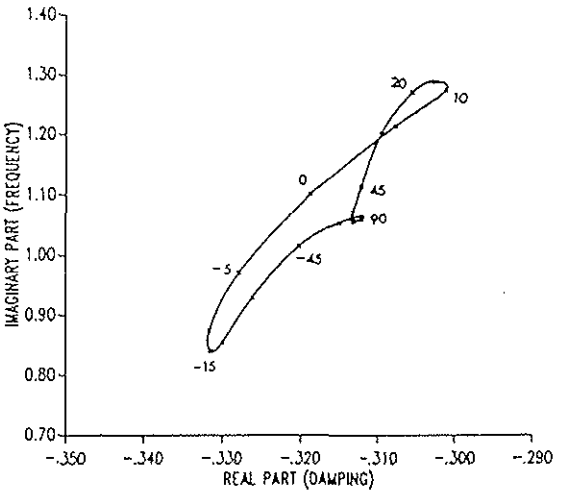

Figure 17: Root locus of first flap eigenvalues as a function of ply angle in horizontal wall for single-cell composite blade.

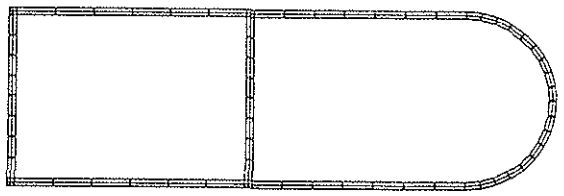

Figure 19: 2-D finite element model for two-cell composite blade cross-section analysis

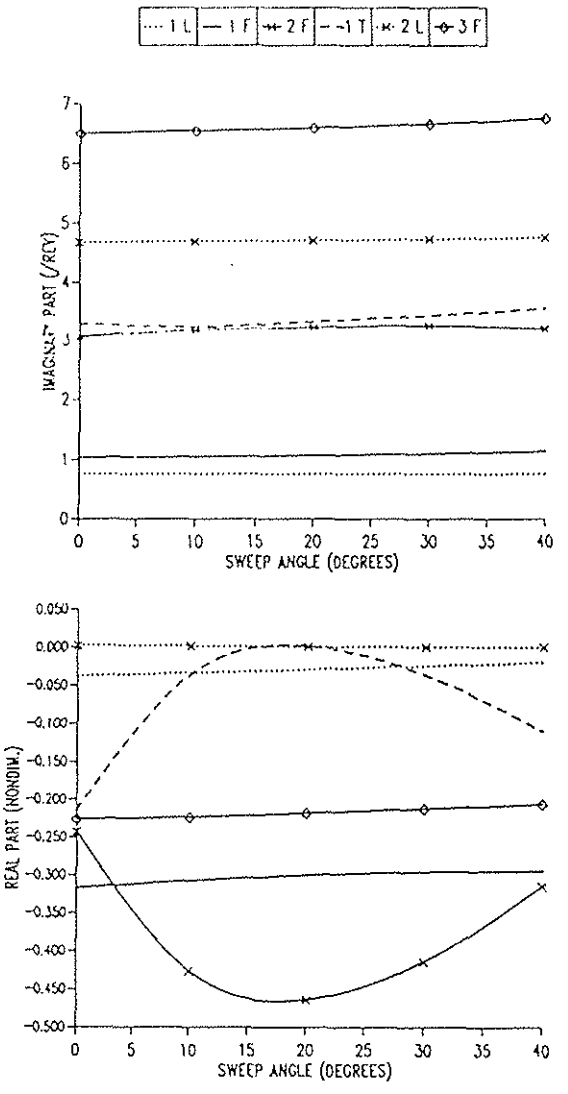

Figure 20: Effect of tip sweep on the aeroelastic stability of the two-cell composite blade, baseline configuration.
(a) imaginary part of eigenvalues
(b) real part of eigenvalues

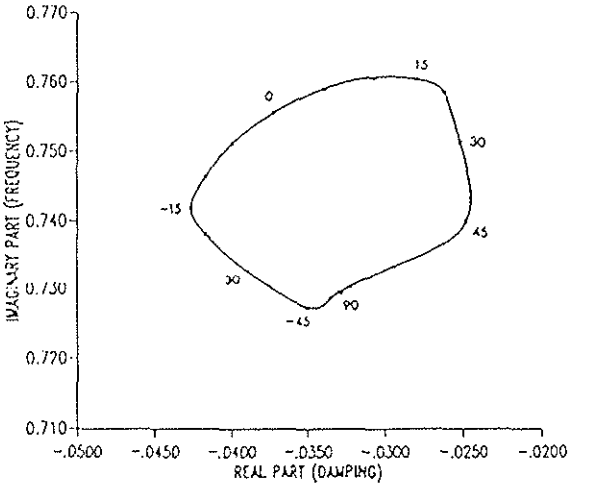

Figure 21: Root locus of first lag eigenvalues as a function of ply angle in vertical wall for two-cell composite blade.

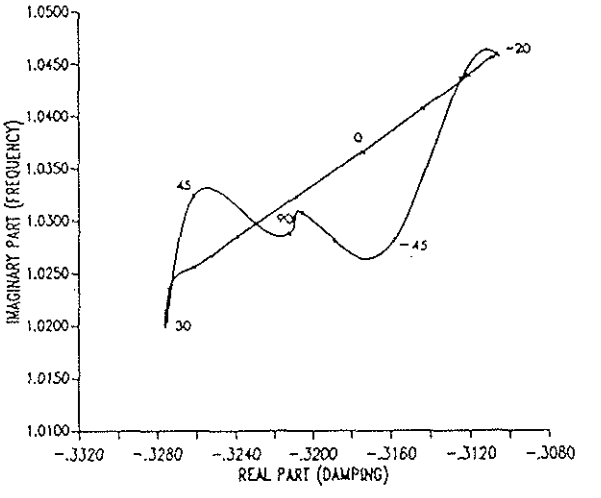

Figure 22: Root locus of first flap eigenvalues as a function of ply angle in vertical wall for two-cell composite blade.

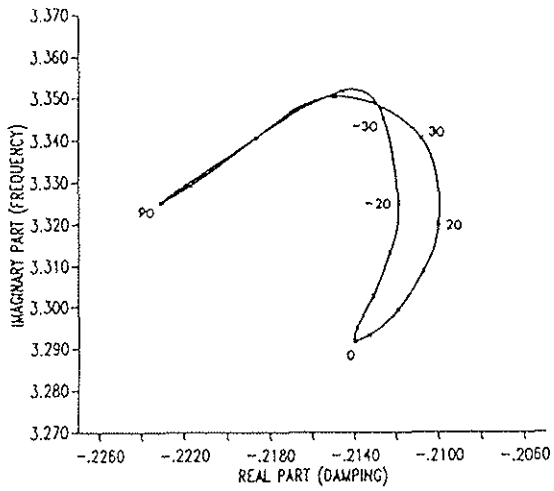

Figure 23: Root locus of first torsion eigenvalues as a function of ply angle in vertical wall for two-cell composite blade.

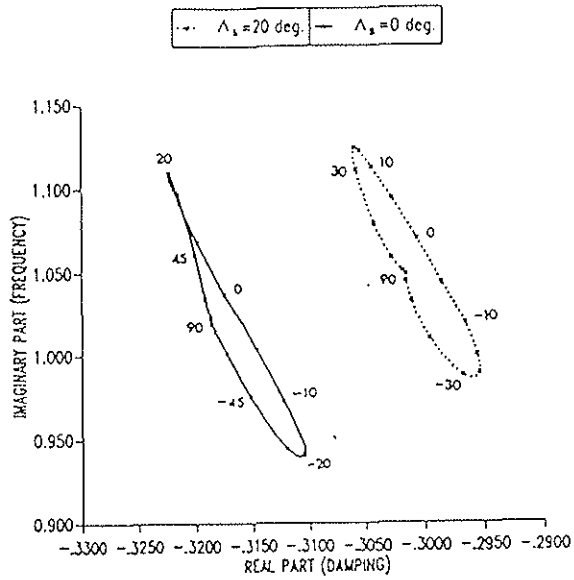

Figure 25: Root locus of first flap eigenvalues as a function of ply angle in horizontal wall for two-cell composite blade.

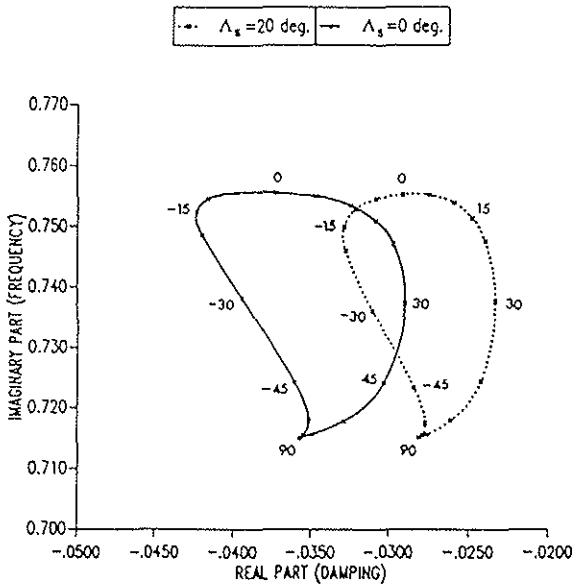

Figure 24: Root locus of first lag eigenvalues as a function of ply angle in horizontal wall for two-cell composite blade.

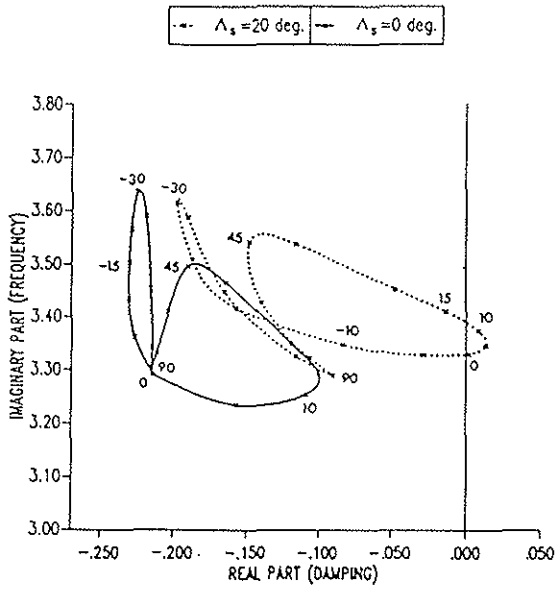

Figure 26: Root locus of first torsion eigenvalues as a function of ply angle in horizontal wall for two-cell composite blade.

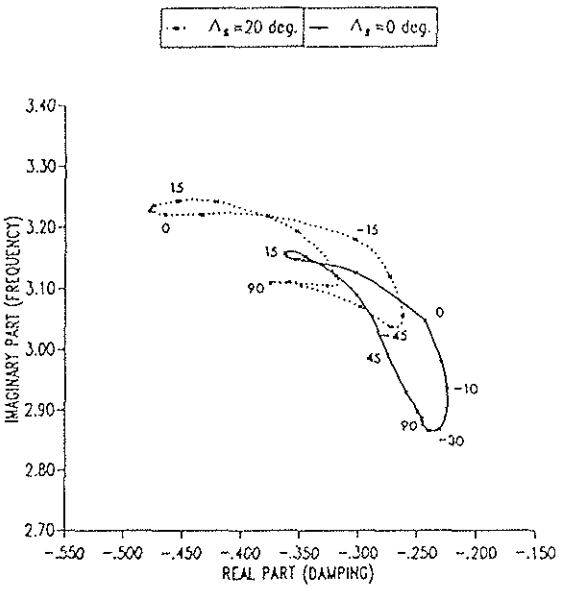

Figure 27: Root locus of second flap eigenvalues as a function of ply angle in horizontal wall for two-cell composite blade.